The MAGPI Survey: forward modelled gas-phase metallicity gradients in galaxies at z ~ 0.3

Mai, Y.; Croom, S.M.; Wisnioski, E.; Battisti, A.J.; Mendel, J.T.; Mun, M.; ... ; Ziegler, B.

Monthly Notices of the ROYAL ASTRONOMICAL SOCIETY

MNRAS **545,** 1–18 (2026) https://doi.org/10.1093/mnras/staf2182
Advance Access publication 2025 December 10

The MAGPI Survey: forward modelled gas-phase metallicity gradients in galaxies at $z \sim 0.3$

Yifan Mai [1,2,3,4★] Scott M. Croom [1,3] Emily Wisnioski [3,5] Andrew J. Battisti [3,5,6] J. Trevor Mendel [3,5] Marcie Mun [3,5] Caroline Foster [3,7] Katherine E. Harborne [8,9,10] Claudia D. P. Lagos [3,6] Iris Breda [11] Tianmu Gao [3,5] Kathryn Grasha [3,5†] Tamal Mukherjee [4,12] Adriano Poci [13] Rhea-Silvia Remus [14] Piyush Sharda [15] Sarah M. Sweet [3,16] Sabine Thater [11] Lucas M. Valenzuela [14] Glenn van de Ven [11] Tayyaba Zafar [12] and Bodo Ziegler [11]

[1]*Sydney Institute for Astronomy (SIfA), School of Physics, The University of Sydney, Sydney, NSW 2006, Australia*
[2]*Australian Astronomical Optics, Macquarie University, Sydney, NSW 2109, Australia*
[3]*ARC Centre of Excellence for All Sky Astrophysics in 3 Dimensions (ASTRO 3D), Canberra, ACT 2611, Australia*
[4]*Astrophysics and Space Technologies Research Centre, Macquarie University, Sydney, NSW 2109, Australia*
[5]*Research School of Astronomy and Astrophysics, Australian National University, Canberra, ACT 2611, Australia*
[6]*International Centre for Radio Astronomy (ICRAR), M468, The University of Western Australia, 35 Stirling Highway, Crawley, WA 6009, Australia*
[7]*School of Physics, University of New South Wales, Sydney, NSW 2052, Australia*
[8]*Institute for Computational Cosmology, Durham University, South Road, Durham DH1 3LE, UK*
[9]*Centre for Extragalactic Astronomy, Durham University, South Road, Durham DH1 3LE, UK*
[10]*Department of Physics, Durham University, South Road, Durham DH1 3LE, UK*
[11]*Department of Astrophysics, University of Vienna, Türkenschanzstraße 17, A-1180 Vienna, Austria*
[12]*School of Mathematical and Physical Sciences, Macquarie University, Sydney, NSW 2109, Australia*
[13]*Sub-Department of Astrophysics, University of Oxford, Oxford OX1 3RH, UK*
[14]*Universitäts-Sternwarte, Fakultät für Physik, Ludwig-Maximilians-Universität München, Scheinerstr. 1, D-81679 München, Germany*
[15]*Leiden Observatory, Leiden University, PO Box 9513, NL-2300 RA Leiden, the Netherlands*
[16]*School of Mathematics and Physics, University of Queensland, St Lucia, Queensland 4072, Australia*

Accepted 2025 December 4. Received 2025 December 3; in original form 2025 August 29

ABSTRACT

We measure the seeing-deconvolved gas-phase metallicity gradients of 70 star-forming galaxies at $z \sim 0.3$ from the MAGPI survey and investigate their relationship with galaxy properties to understand the mechanisms that influence the distribution of metals and shape the evolution of the galaxies. We use a Bayesian modelling technique, BLOBBY3D, which accounts for seeing effects (beam smearing) and can model the substructures of the flux distribution. The median metallicity gradient of our sample is $\nabla[\mathrm{O/H}] = -0.013^{+0.059}_{-0.033}$ dex kpc^{-1}. Among the galaxies in our sample, 32.9 per cent have negative metallicity gradients (2σ significance), 10.0 per cent have positive gradients and 57.1 per cent have flat gradients. The $\nabla[\mathrm{O/H}]$–M_* relation of the MAGPI galaxies generally agrees with theoretical predictions, where a combination of stellar feedback, gas transport, and accretion shapes the metallicity profile, with the dominant processes varying with galaxy mass. We find a positive correlation between $\nabla[\mathrm{O/H}]$ and gas velocity dispersion ($r = 0.36$), indicating that stronger gas turbulence is associated with flatter or inverted metallicity gradients, likely due to enhanced gas mixing. Additionally, smaller galaxies tend to have flatter or positive gradients, suggesting that metal dilution by gas accretion or removal via feedback-driven winds may outweigh metal enrichment in small galaxies.

Key words: galaxies: abundances – galaxies: evolution – galaxies: formation – galaxies: ISM.

1 INTRODUCTION

Heavy elements, as the products of stellar nucleosynthesis, provide a powerful probe of star formation histories and galaxy evolution. The metal enrichment cycle in galaxies involves several interconnected processes. First, inflows of metal-poor gas from the intergalactic medium (IGM) provide the fresh fuel for star formation but can also dilute the existing metal content of the interstellar medium (ISM; e.g. D. Kereš et al. 2005; R. J. J. Grand et al. 2019; F. Barbani et al. 2025). Star formation then generates new heavy elements, which are returned to the ISM through stellar winds and supernovae. Feedback from massive stars, supernovae, and active galactic nuclei (AGN) can subsequently drive outflows, expelling enriched material and redistributing metals within and beyond galaxies (A. L. Muratov

★ E-mail: yifan.mai@sydney.edu.au
† ARC DECRA Fellow

et al. 2015; P. D. Mitchell et al. 2020; S. Veilleux et al. 2020; R. J. Wright et al. 2024). These competing processes together regulate the chemical evolution of galaxies (e.g. C. Péroux & J. C. Howk 2020; P. Sharda et al. 2024).

The distribution of metals across galaxies therefore provides insight into different galaxy processes. The metallicity gradient of low-redshift galaxies is typically negative (i.e. more metals in the centre than in the outskirts; S. F. Sánchez et al. 2014; F. Belfiore et al. 2017), in agreement with an inside-out formation scenario where galactic discs have primarily formed by *in situ* star formation. In the inside-out formation scenario, the core of a galaxy forms early while the disc builds up through gradual processes, such as accretion or minor mergers (R. B. Larson 1976; J. V. Kepner 1999; L. Portinari & C. Chiosi 1999; S. F. Sánchez et al. 2014; W. M. Baker et al. 2025). Metallicity gradients are also shaped by gas accretion, gas transportation, galactic wind, and galaxy interactions (G. Cresci et al. 2010; L. J. Kewley et al. 2010; D. S. N. Rupke, L. J. Kewley & J. E. Barnes 2010; F. Marinacci et al. 2014; J. Chisholm, C. Tremonti & C. Leitherer 2018). These mechanisms can induce gas mixing, metallicity dilution and redistribution, leading to the flattening or even inversion of gradients. Therefore, measuring the metallicity gradient can offer insights into the interplay between galaxy growth, feedback, and environmental effects (M. Mayor & L. Vigroux 1981; G. Pezzulli & F. Fraternali 2016; F. Collacchioni et al. 2020).

It is not clear which mechanisms dominate in setting metallicity gradients as a function of cosmic time. Simulations do not agree on the relative importance of key parameters that shape metallicity gradients in part due to different treatments of star formation (C. Chiappini, F. Matteucci & D. Romano 2001; J. Fu et al. 2009; K. Pilkington et al. 2012), feedback (C. Kobayashi & N. Nakasato 2011; B. K. Gibson et al. 2013; X. Ma et al. 2017; Z. S. Hemler et al. 2021; R. M. Yates et al. 2021), and accretion (M. Mollá & A. I. Díaz 2005; X. Ma et al. 2017; P. B. Tissera et al. 2022; X. Sun et al. 2025). Observations of high-redshift galaxies provide constraints on metallicity gradient evolution (J. Queyrel et al. 2012; X. Wang et al. 2022; G. Venturi et al. 2024; M. Ju et al. 2025; Z. Li et al. 2025). However, compilations of observational results across $z \sim 0$–4 (e.g. M. Curti et al. 2020) reveal substantial scatter, with most measurements consistent with no significant gradient, while some exhibit positive gradients. If confirmed, the variation of metallicity gradients at high redshift ($z \gtrsim 1$) suggests the relative importance of mechanisms may be different to local galaxies. Positive gradients, which are rare at low redshift, may result from strong gas accretion that dilutes the metallicity at the galaxy centre (e.g. G. Cresci et al. 2010; J. Queyrel et al. 2012; J. P. Stott et al. 2014). The flatter gradients found at high redshift may also result from more regular metal-poor gas inflows (X. Sun et al. 2025), strong feedback (X. Ma et al. 2017; X. Sun et al. 2025), or mergers (P. Troncoso et al. 2014; L. Vallini et al. 2024; G. Venturi et al. 2024). Studies of gas kinematics have shown that, on average, the gas turbulence in higher redshift galaxies is higher than at lower redshift (S. A. Kassin et al. 2012; E. Wisnioski et al. 2015; H. Übler et al. 2019; Y. Mai et al. 2024). However, recent observations have detected dynamically cold, rotationally supported discs at high redshift (F. Rizzo et al. 2021; E. Parlanti et al. 2023), suggesting that galaxy mass may play an important role in maintaining such discs (A. B. Gurvich et al. 2023; M. Kohandel et al. 2024). This suggests that the large scatter of metallicity gradients at high redshift could be connected, in part, to strong gas mixing driven by stellar feedback as well as gas transport and accretion, and that the efficiency of these processes may vary with galaxy mass (P. Sharda et al. 2021b, 2024).

However, making consistent measurements of metallicity gradients across cosmic time is challenging. Some amount of scatter and flattening amongst gradient measurements are likely due to observational effects and measurement biases. For example, different observational studies report varying degrees of scatter in the metallicity gradient in high redshift galaxies (e.g. E. Wuyts et al. 2016; D. Carton et al. 2018; M. Curti et al. 2020; S. Gillman et al. 2021). Systematic differences in sample selection (e.g. stellar mass range) and measurement methods, such as the choice of metallicity diagnostic (H. Poetrodjojo et al. 2021) and the treatment of seeing, or beam smearing, likely also contribute to the observed scatter. Beam smearing flattens both positive and negative intrinsic metallicity gradients, with the degree of flattening increasing at lower angular resolution, i.e. larger point-spread function (PSF), and for smaller or more inclined galaxies (T. T. Yuan, L. J. Kewley & J. Rich 2013; J. P. Stott et al. 2014; E. Wuyts et al. 2016; F. Belfiore et al. 2017; A. Acharyya et al. 2020). These constraints are particularly relevant at higher redshifts where observations are often limited by angular resolution and surface brightness.

The measurement of metallicity gradients is also influenced by the clumpiness of gas (F. Belfiore et al. 2017; H. Poetrodjojo et al. 2019; B. Metha, M. Trenti & T. Chu 2021; B. Metha et al. 2022). Clumpy gas can lead to enhanced star formation in local areas, which increases the intrinsic scatter of the metallicity distribution. The inferred metallicity of clumpy galaxies, especially at low spatial resolution, may be biased towards bright H II regions, affecting the overall gradient (e.g. D. Carton et al. 2017). Models that assume a smooth radial flux distribution cannot fully capture the spatial variance of the metallicity distribution for galaxies with complex substructures.

In fact, most published metallicity gradients do not take beam smearing into account when modelling the flux distribution. Some studies have applied generalized corrections based on simple smooth models (e.g. E. Wuyts et al. 2016). Uniquely, D. Carton et al. (2017) presented a forward modelling approach. Here, we build on the results of D. Carton et al. (2017) to obtain a seeing-deconvolved metallicity distribution *which captures the substructures in emission line flux*. This requires a modelling technique with more flexibility in reproducing realistic flux distributions. We use BLOBBY3D (M. R. Varidel et al. 2019), which employs a forward modelling technique that accounts for beam smearing and models the gas kinematics and spatial substructures simultaneously. This approach allows us to analyse the relationship between metallicity distribution and seeing-deconvolved gas turbulence, which can also be affected by beam smearing (R. Davies et al. 2011; N. Bouché et al. 2015; E. M. Di Teodoro & F. Fraternali 2015; M. Kohandel et al. 2020; F. Rizzo et al. 2022; Y. Mai et al. 2024).

In this study, we measure the gas-phase metallicity gradients of star-forming (SF) galaxies and aim to understand the mechanisms related to the metallicity distribution at $z \sim 0.3$. This redshift represents a key transitional epoch between the well-studied local and high-redshift Universe, providing critical insights into the evolution of gas kinematics (e.g. E. Wisnioski et al. 2015; Y. Mai et al. 2024) and metallicities (e.g. P. Sharda et al. 2021a). Moreover, the high spatial resolution achieved in the MAGPI observations (PSF ≈ 0.6 arcsec, corresponding to $\approx$2.7 kpc at $z = 0.3$) allows us to probe metallicity gradients at spatial scales comparable to those of local Integral Field Unit (IFU) surveys (e.g. the MaNGA survey; K. Bundy et al. 2015, with a PSF of $\approx$2.5 arcsec corresponding to $\approx$2.4 kpc at $z = 0.05$), thereby enabling direct comparisons across cosmic time.

We arrange the rest of the paper as follows: in Section 2, we introduce the MAGPI survey and our sample selection. In Section 3,

we introduce the method we use to model the flux distribution and calculate the metallicity and metallicity gradients. In Section 4, we demonstrate the results for the metallicity gradients of the SF MAGPI galaxies and their correlation with other galaxy properties. In Section 5, we discuss the evolution of metallicity gradients and the mechanisms that relate to metallicity distribution. In Section 6, we summarize our results.

Throughout this paper, we assume a G. Chabrier (2003) stellar initial mass function (IMF) and adopt a concordance cosmology ($\Omega_\Lambda = 0.7$, $\Omega_m = 0.3$, $H_0 = 70\,\mathrm{km\,s^{-1}\,Mpc^{-1}}$).

2 DATA

2.1 The MAGPI survey

The Middle Ages Galaxy Properties with Integral field spectroscopy (MAGPI) survey (C. Foster et al. 2021) focuses on galaxies at a lookback time of 3–4Gyr ($z \sim 0.3$). The survey uses the Multi Unit Spectroscopic Explorer (MUSE; R. Bacon et al. 2010) with Ground Layer Adaptive Optics, mounted on the UT4 of the Very Large Telescope (VLT). MAGPI uses the wide-field mode of MUSE, which has a $1 \times 1\,\mathrm{arcmin}^2$ field-of-view (FOV) sampled at $0.2 \times 0.2\,\mathrm{arcsec}^2$. The typical full width at half maximum (FWHM) of the MAGPI observations PSF is $\sim$0.6 arcsec. The MAGPI survey covers a wavelength range between 4700 and 9351 Å with a spectral resolution of $R = 2728$ at 7025 Å.

The MAGPI survey targets 60 massive central galaxies (primary galaxies) and their neighbours (secondary galaxies) within the MUSE FOV. The selection of MAGPI primary galaxies required that galaxies uniformly sample a range of environments (isolated, groups and clusters), covering a halo mass range $11.35 \leq \log(M_{\mathrm{halo}}/\mathrm{M}_\odot) \leq 15.35$. The halo masses are taken from the Galaxy And Mass Assembly (GAMA) group catalogue (A. S. G. Robotham et al. 2011), where group halo masses are estimated by dynamical masses based on group size and velocity dispersion, and then calibrated against mock galaxy catalogues derived from N-body simulations (see section 4.3 in A. S. G. Robotham et al. 2011). 56 primary galaxies were selected from the GAMA survey (S. P. Driver et al. 2011) G12, G15 and G23 fields. The remaining four primary galaxies were obtained from MUSE archival observations of Abell 370 and Abell 2744. At the time of writing, the survey has completed the observation of all 56 fields, which have been fully reduced with relevant data products. However, only 53 fields selected from the GAMA survey are used in this study, as the observation and reduction of the remaining fields were completed after the analysis presented here was finalised. There are 332 SF galaxies that have Hα-based star formation rate (SFR) measurements at redshift $0.26 < z < 0.42$.

We utilize the Galaxy IFU Spectroscopy Tool (GIST; A. Bittner et al. 2019) to fit the observed (seeing-convolved) emission lines and continuum spectra in MAGPI galaxies (Battisti et al., in preparation). GIST is a PYTHON wrapper that implements the Penalized PiXel-Fitting (pPXF; M. Cappellari & E. Emsellem 2004; M. Cappellari 2017) and the 'Gas and Absorption Line Fitting' (GANDALF; J. Falcón-Barroso et al. 2006; M. Sarzi et al. 2006) method on integral field spectroscopy (IFS) data. The stellar continuum fits are conducted on a spaxel level. The stellar continuum is fit using the SSP_MIST_C3K_SALPETER templates (C. Conroy, J. E. Gunn & M. White 2009; C. Conroy & J. E. Gunn 2010; C. Conroy, M. White & J. E. Gunn 2010), which are based on the Modules for Experiments in Stellar Astrophysics (MESA) Isochrones and Stellar Tracks (MIST; J. Choi et al. 2016), and the lines are masked at that step. The stellar continuum models span a grid of ages and metallicities, comprising 107 age steps covering $\log(\mathrm{age/yr}) = 5.0$–$10.3$ in increments of 0.05, and 12 metallicity steps spanning $\log(Z/Z_\odot) = [-2.5, 0.5]$, where $Z_\odot$ is solar metallicity. The emission lines are fit using single-component Gaussian functions where all line kinematics are tied together.

The stellar masses are determined using PROSPECT (A. S. G. Robotham et al. 2020), which is an energy balance spectral energy distribution (SED) fitting code. Photometry from GAMA imaging over the $ugriZYJHK$ bands is employed for the PROSPECT SED fitting, assuming a G. Chabrier (2003) IMF. We note that the photometric data have a wider spectral coverage into the near-infrared than the MAGPI data, providing more robust estimates for the stellar mass. Stellar population templates from G. Bruzual & S. Charlot (2003) are utilized to create an unattenuated stellar SED, and the dust attenuation law by S. Charlot & S. M. Fall (2000) is applied to correct for dust attenuation, following the methodology described in Section 3 of S. Bellstedt et al. (2020). We use the tool GALFIT (C. Y. Peng et al. 2002) to estimate the effective radius (R_e) of the galaxies from synthetic i-band images generated from the MUSE data. GALFIT accounts for the PSF and models the two-dimensional surface brightness distribution assuming a single Sérsic component (J. L. Sérsic 1963). The stellar mass surface density (Σ_{M_*}) is calculated as $\Sigma_{M_*} = M_*/(2\pi R_\mathrm{e}^2)$.

The ionized gas velocity dispersion (σ_gas), which traces the strength of gas turbulence, is measured using BLOBBY3D and taken from Y. Mai et al. (2024). This value includes both the turbulent and thermal components of the gas motion. Beam smearing due to the atmosphere broadens the observed gas velocity dispersion, especially for galaxies with a steep velocity gradient. BLOBBY3D can measure the intrinsic σ_gas by forward-modelling the gas kinematics and spatial gas distribution simultaneously accounting for beam smearing from the PSF. Additionally, we extract the rotational velocity at one effective radius (v_ϕ) for each galaxy from the same BLOBBY3D models. The details of BLOBBY3D are introduced in Section 3.

We use the dust-corrected Hα flux maps to derive SFR using the calibration of J. Kennicutt (1998). We correct the dust extinction using the Balmer decrement on a spaxel by spaxel basis (see details in Section 3.3 and M. Mun et al. 2024). The extinction curve from E. L. Fitzpatrick et al. (2019) is adopted with $R_V = 3.1$. The SFR surface density (Σ_SFR) is calculated as $\Sigma_\mathrm{SFR} = \mathrm{SFR}/(2\pi R^2_{\mathrm{e,H}\alpha})$, in which SFR is the total integrated SFR, and $R_{\mathrm{e,H}\alpha}$ is the half-light radius of the Hα map, which is used to better trace the star formation region. The star formation main sequence (SFMS) is defined as the linear best fit to the MAGPI galaxies at $0.25 \leq z \leq 0.424$ (M. Mun et al. 2024).

2.2 Sample selection

We select galaxies in the redshift range $0.26 < z < 0.42$, ensuring that the emission lines we use for gas-phase metallicity diagnostics and dust extinction correction fall within the wavelength coverage of the MAGPI survey. These emission lines include [O II]λ3727, λ3729, Hβ, Hα, and [N II]λ6584. We remove galaxies with evidence of AGN activity to avoid AGN contamination of the metallicity measurements. We use the Baldwin, Phillips & Terlevich (BPT; J. A. Baldwin, M. M. Phillips & R. Terlevich 1981; L. J. Kewley et al. 2001; G. Kauffmann et al. 2003) ionization diagnostic diagrams to classify spaxels as SF, AGN, and composite. Only spaxels with a S/N greater than 3 in all relevant emission lines are included in the BPT classification. Galaxies hosting AGN or composite central regions were excluded based on spatially resolved BPT classification maps. Specifically, we removed galaxies where more than five contiguous

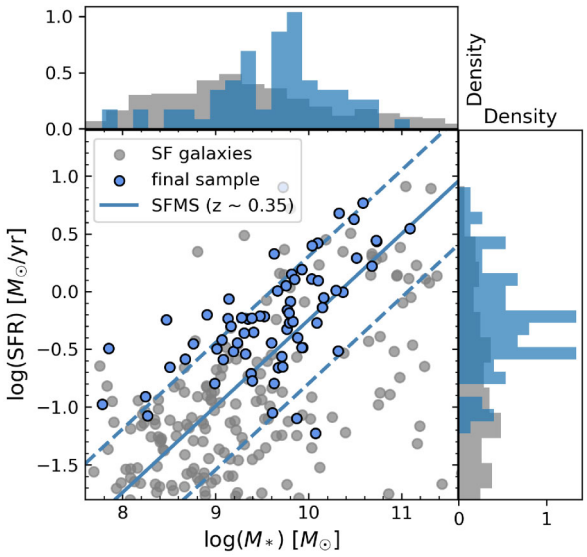

Figure 1. The distribution of H α-based SFR and M_* for all SF galaxies and galaxies in our final sample. The solid line represents the SFMS for galaxies at $z \sim 0.35$, with the dashed lines representing the root-mean-square error of SFMS (M. Mun et al. 2024).

central spaxels (corresponding to one PSF area) fall within the AGN or composite region of the BPT diagram. Galaxies with only isolated AGN/composite spaxels were retained, as such cases are likely due to noise. We note that this cut removes the most massive galaxies ($M_* \sim 10^{11}$ M$_\odot$), which more likely have central AGN/composite region. We select galaxies with metallicity measurements extending to at least twice the PSF FWHM (PSF$_{\rm FWHM}$), ensuring robust metallicity gradient estimates. We note that this criterion preferentially removes galaxies with low SFR that lack sufficiently extended line emission at large radii. There are 70 galaxies in our sample after applying the above cuts (full list in Appendix B). We show the distribution of SFR and M_* for galaxies in our final sample in Fig. 1.

3 METHODS

We use BLOBBY3D[1] (M. R. Varidel et al. 2019) to model the spatial flux distribution of the emission lines we used for metallicity diagnostics. BLOBBY3D is designed to perform Bayesian inference on gas kinematics from emission line observations of galaxies using IFS. It can model the gas spatial substructure and kinematics simultaneously, accounting for the PSF and line spread function (LSF), and assuming a continuous velocity profile defined by the S. Courteau (1997) empirical model and a constant velocity dispersion across the disc. BLOBBY3D models the gas distribution as a sum of Gaussian components (blobs), without assuming a pre-defined flux distribution profile for the galaxy. The number of blobs is flexible (typically in the range of $\sim$ 1–300), and the position, shape and flux of each blob are also flexible and depend on the complexity of the observed gas substructure. This method can model complex gas substructures such as rings, spiral arms and individual clumps, which are difficult to model using methods that assume a parametric radial flux distribution. For example, ^{3D}BAROLO (E. M. Di Teodoro & F. Fraternali 2015) adopts a concentric tilted-ring model, in which the galaxy is represented by a set of co-centric rings with varying flux. This approach is less flexible than BLOBBY3D. However, ^{3D}BAROLO may perform more robustly on data with lower S/N due to its simpler parametric framework.

BLOBBY3D uses a diffusive nested sampling algorithm, DNEST4 (B. J. Brewer, L. B. Pártay & G. Csányi 2011; B. J. Brewer & D. Foreman-Mackey 2018), which is an effective variant of nested sampling (J. Skilling 2004). DNEST4 uses Markov chain Monte Carlo to explore the complex posterior distribution and compute the normalization constant. The key advantage of DNEST4 over other sampling algorithms is its effectiveness in handling high-dimensional parameter spaces and multimodal distributions, which is a useful feature for modelling complex gas substructures.

An inference problem with a varying number of components is normally difficult to explore. DNEST4 has an in-built reversible jump object that allows variations to the number of blobs/components. BLOBBY3D uses the reversible jump to add or remove blobs from the model, which enables the number of blobs to be a flexible parameter depending on the complexity of the galaxy flux distribution. See table 1 in M. R. Varidel et al. (2019) for more details about all hyperparameters and parameters used in the model.

3.1 Metallicity diagnostics

We use the [N II]/[O II] ratio (N2O2), based on [N II]λ6584 and [O II]$\lambda\lambda$3727, 3729 lines, as our primary gas-phase metallicity diagnostic. N2O2 is the most reliable metallicity diagnostic in the optical spectrum as it is less sensitive to ionization parameter and the ISM pressure. Note that N2O2 can be more sensitive to the ionization parameter at lower metallicities (see the review by L. J. Kewley, D. C. Nicholls & R. S. Sutherland 2019, hereafter K19).

We use the metallicity diagnostic calibration outlined in K19. The gas-phase metallicity is calculated as

$$\begin{aligned} 12 + \log(\mathrm{O/H}) = {} & 9.4772 + 1.1797 \cdot x + 0.5085 \cdot y \\ & + 0.6879 \cdot x \cdot y + 0.2807 \cdot x^2 + 0.1612 \cdot y^2 \\ & + 0.1187 \cdot x \cdot y^2 + 0.1200 \cdot y \cdot x^2 \\ & + 0.2293 \cdot x^3 + 0.0164 \cdot y^3 \,, \end{aligned} \quad (1)$$

where $12 + \log(\mathrm{O/H})$ is the gas-phase metallicity, x is the metallicity diagnostic ratio

$$x = \log\left(\frac{F_{\rm int}([\mathrm{N\,II}]\,\lambda6584)}{F_{\rm int}([\mathrm{O\,II}]\,\lambda3727) + F_{\rm int}([\mathrm{O\,II}]\,\lambda3729)}\right)$$

for the N2O2 diagnostic. $F_{\rm int}$ is the intrinsic flux after dust extinction correction of a given emission line (see Section 3.3 for more details). y is the dimensionless ionization parameter $\log(U)$. Here, we adopt $\log(U) = -3.17$. We note that a reasonable range of values ($-3.98 < \log(U) < -1.98$) makes little difference (K19).

We use the [N II]λ6584/H α ratio (N2H α) to measure the metallicity as a comparison (P04; M. Pettini & B. E. J. Pagel 2004). The advantage of this diagnostic is that the separation between [N II] and H α emission lines is small, thus there is no need to make a dust extinction correction for the line ratio calculation, which may introduce more uncertainty, especially when the H β line is weak. It is also an advantage for observations at $z > 0.5$ when obtaining multiple optical line groups from ground-based facilities is often time prohibitive. However, the N2H α diagnostic is *more* sensitive to the ionization parameter and ISM pressure than the N2O2 diagnostic (K19). The gas-phase metallicity using N2H α is calculated as

$$12 + \log(\mathrm{O/H}) = 9.37 + 2.03 \cdot x + 1.26 \cdot x^2 + 0.32 \cdot x^3, \quad (2)$$

[1] https://github.com/SpaceOdyssey/Blobby3D

where

$$x = \log\left(\frac{F_{\rm int}([\rm N\,II]\,\lambda6584)}{F_{\rm int}(\rm H\,\alpha)}\right).$$

The P04 calibration is derived from direct T_e-based abundances and therefore does not explicitly depend on the ionization parameter; instead, it assumes that the ionization conditions of the target H II regions are similar to those of the calibration sample.

We also measure the N2Hα metallicity using the calibration functional form from K19. We adopt the functional form from P04 for our main analysis, as it has a larger valid range (valid over $7.17 < 12 + \log(\rm O/H) < 8.86$) compared to the K19 calibration (valid over $7.6 < 12 + \log(\rm O/H) < 8.53$). The average difference in metallicity gradients between N2H$\alpha_{\rm P04}$ and N2H$\alpha_{\rm K19}$ in our sample is only 0.0016 dex kpc^{-1}. Therefore, the choice of calibration functional form does not affect our conclusions.

3.2 Modelling the flux distribution

BLOBBY3D requires a single, continuous wavelength range for input spectra. It does not support the inclusion of multiple disjoint wavelength intervals, meaning that any analysis requiring non-contiguous spectral regions must be performed separately. BLOBBY3D is computationally expensive, making it impractical to fit a large wavelength range that simultaneously includes Hα, [N II], and [O II]. To optimize computational efficiency, we first fit the spectrum covering Hα and [N II], as these lines are close in wavelength. Although [N II] is relatively weak, Hα provides a strong constraint on the kinematics. We then fit a separate spectral range that includes [O II].

To model the flux of Hα and [N II], we select the rest-frame wavelength range [6535, 6595] Å of the cube, which covers Hα and [N II]$\lambda\lambda$6548, 6584. We subtract the stellar continuum from the spectrum using the output from GIST, as BLOBBY3D requires the input datacube to be continuum subtracted. The blobs for Hα and [N II]have the same shape and position. BLOBBY3D performs inferences for the Hα flux and the [N II]/Hα flux ratio for each blob (spatial Gaussian flux profile). The flux ratio between the two [N II] lines is assumed to be $F_{6584}/F_{6548} = 3$ (A. Acker et al. 1989). We tie together the velocity and dispersion of H α and both [N II] lines, such that all three lines share the same kinematic parameters.

We then model the flux of [O II]$\lambda\lambda$3727, 3729 using the data in the rest-frame wavelength range [3718, 3738] Å. The flux ratio between [O II]λ3727 and [O II]λ3729 is set to be flexible for each blob. We constrain the kinematic model of [O II] to have the same position angle (PA) as Hα using the average PA we obtain from the inference of Hα. This PA constraint is under the assumption that all gas components rotate in the same direction. The flux distribution (the number, position and shape of blobs) of [O II] is modelled independently from Hα, however we notice that in practice the two lines show similar spatial flux distributions in the majority of galaxies.

We calculate the standard deviation of the flux from the posterior effective samples of BLOBBY3D and use it as flux uncertainty. The uncertainty in metallicity is then derived from the flux uncertainty through error propagation.

BLOBBY3D requires the FWHM of PSF and LSF as inputs. The PSF for the MAGPI survey is reconstructed from information generated by the adaptive optics system (T. Fusco et al. 2020; Mendel et al., in preparation). The LSF is measured by fitting Gaussian profiles to isolated bright sky lines (R. Bacon et al. 2017, Mendel et al., in preparation). We use the PSF of the MUSE-derived Z band when we model the Hα and [N II] lines, as the Z-band is close to the wavelength of H α at $z \sim 0.3$. We use the PSF of the MUSE-derived g band when we model the [O II] lines. We adopt the FWHM of the LSF at $6563 \cdot (1+z)$ Å when we model the Hα and [N II] lines, where z is the redshift of the galaxy. We adopt the FWHM of LSF at $3728 \cdot (1+z)$ Å when we model the [O II] lines.

We also test other levels of constraints on the kinematics for [O II] modelling, including (1) no constraints on the kinematics; (2) using the posterior of the PA from Hα as a prior for the PA from [O II]; (3) constraining both the PA and the velocity profile of [O II] to be the same as Hα; (4) constraining the PA, velocity profile and velocity dispersion to be the same as Hα. The results show that the [O II] flux distribution does not vary significantly between different constraints and they do not change the results on the metallicity gradient. Previous studies suggested that the velocity and the velocity dispersion measured from different emission lines may be different (e.g. R. C. Levy et al. 2018; D. R. Law et al. 2022; S. Thater et al. 2022; H. Übler et al. 2024). We therefore adopt the simplest constraint, constraining the PA from [O II] the same as that from Hα, to improve our modelling and allow the flexibility of the velocity profile and velocity dispersion.

Different kinematics for various emission lines may indicate that they are not emitted from the same regions, which may influence the accuracy of the metallicity measurement. Therefore, measuring the metallicity using multiple diagnostics is crucial for assessing systematic differences and ensuring consistency across different methods.

3.3 Extinction correction

The flux of emission lines is attenuated by the dust in the ISM in the Milky Way and the source galaxy. The strength of dust attenuation is wavelength dependent, which causes a biased flux ratio if two emission lines are widely separated. To get the intrinsic flux of emission lines, we perform two steps of dust attenuation correction, to correct the extinction from the Milky Way and the source galaxy using the DUST_EXTINCTION PYTHON package (K. Gordon 2024).

First, we correct the foreground extinction from the dust in the Milky Way using

$$F_{\rm MWcorr}\left(\lambda_{\rm red}\right) = F_{\rm obs}\left(\lambda_{\rm red}\right) \cdot 10^{0.4 \cdot k(\lambda_{\rm red}) \cdot E(B-V)_{\rm MW}}, \quad (3)$$

where $F_{\rm MWcorr}$ is the flux of a given emission line after the Milky Way dust extinction correction, $\lambda_{\rm red}$ is the redshifted wavelength of the emission line, $F_{\rm obs}$ is the observed flux of the emission line, k is the extinction curve from E. L. Fitzpatrick et al. (2019) with $R_V = 3.1$, and $E(B-V)_{\rm MW}$ is the reddening value due to the dust in Milky Way (E. F. Schlafly & D. P. Finkbeiner 2011).

Then, we correct the intrinsic extinction due to the dust from the source galaxy using

$$F_{\rm int}\left(\lambda_{\rm res}\right) = F_{\rm MWcorr}\left(\lambda_{\rm res}\right) \cdot 10^{0.4 \cdot k(\lambda_{\rm res}) \cdot E(B-V)_{\rm int}}, \quad (4)$$

where $F_{\rm int}$ is the intrinsic flux of a given emission line, $\lambda_{\rm res}$ is the rest-frame wavelength of the emission line, and $E(B-V)_{\rm int}$ is the intrinsic reddening value due to the dust in the source galaxy. We calculate $E(B-V)_{\rm int}$ for each spaxel, as follows,

$$E\left(B-V\right)_{\rm int} = \frac{\log_{10}\left(\frac{(\rm H\alpha/H\beta)_{\rm MWcorr}}{(\rm H\alpha/H\beta)_{\rm int}}\right)}{\left(0.4\left(k(\rm H\beta) - k(\rm H\alpha)\right)\right)}, \quad (5)$$

where $(\rm H\alpha/H\beta)_{\rm MWcorr}$ is the ratio of observed Hα and Hβ flux (Balmer decrement) after foreground extinction correction,

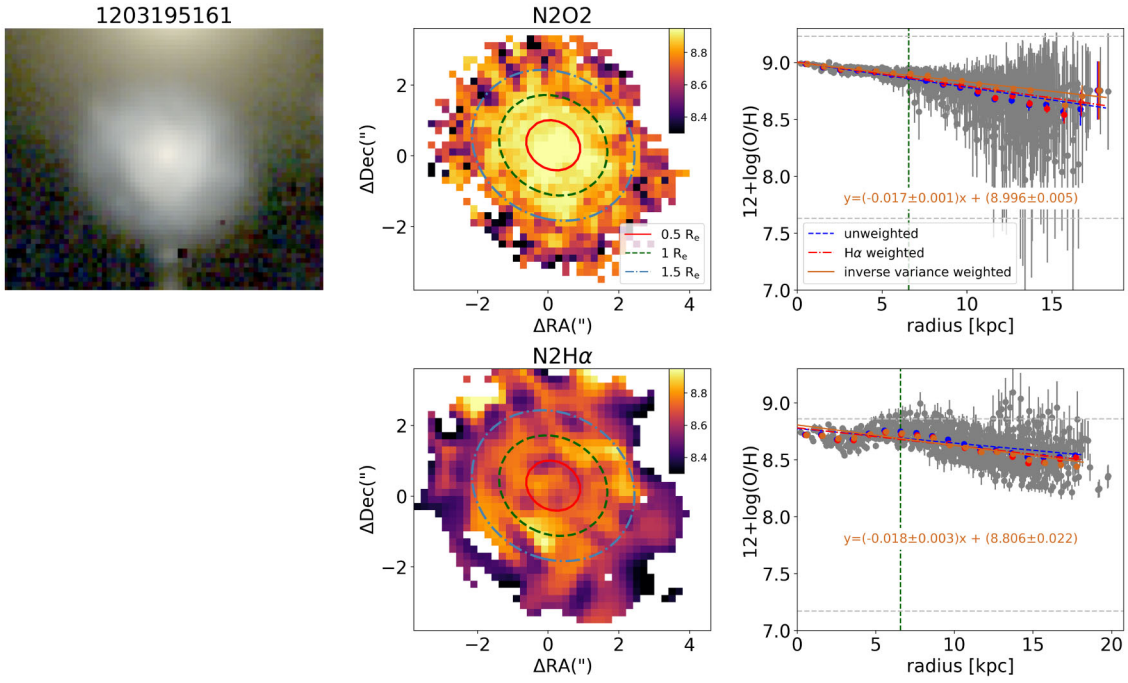

Figure 2. The metallicity and metallicity gradient measurement for an example galaxy (MAGPIID 1203195161). The top-left panel shows a colour composite image of the galaxy, constructed from the i, r, and g-band data. The first row shows the metallicity measured using the N2O2 diagnostic and the second row uses the N2Hα diagnostic. The middle panels show the seeing-deconvolved metallicity map. The right panels demonstrate the metallicity of each spaxel as a function of radius and the average metallicity in each 0.5 $\mathrm{PSF_{FWHM}}$ bin for three different weight methods. We overplot the linear best fits for each method. The horizontal lines in the right panels denote the valid metallicity range for each diagnostic (M. Pettini & B. E. J. Pagel 2004; K19). The vertical lines denote 1 R_e for this galaxy. We show the value of the metallicity gradient and central metallicity (the inverse variance weighted method) for each plot.

$(\mathrm{H}\alpha/\mathrm{H}\beta)_{\mathrm{int}}$ is the intrinsic ratio of Hα and Hβ and we adopt $(\mathrm{H}\alpha/\mathrm{H}\beta)_{\mathrm{int}} = 2.86$ for case B recombination (D. E. Osterbrock 1989). $k(\mathrm{H}\beta)$ and $k(\mathrm{H}\alpha)$ are the k value from the extinction curve from E. L. Fitzpatrick et al. (2019) for Hα and Hβ, respectively.

We calculate the Balmer decrement using the Hα and Hβ flux measurement from the GIST output. We note that it would be better to implement the Balmer decrement into the prior in BLOBBY3D to take the seeing-deconvolved structure of dust into account. However, such an implementation involves complex modifications of BLOBBY3D and a detailed investigation of dust attenuation effects, which is beyond the scope of this paper.

3.4 Metallicity gradient measurement

For the N2O2 diagnostic, [N II] and [O II] are modelled independently due to their large wavelength separation. Because the recovered blobs are not in one-to-one correspondence, we construct a seeing-deconvolved flux map by summing the flux from all blobs for each emission line. We measure the metallicity of each pixel and calculate the average metallicity as a function of radius, by binning the pixels in elliptical annuli with a bin width of 0.5 $\mathrm{PSF_{FWHM}}$. We include only the pixels with S/N $>$ 3 in the [N II], [O II], Hα, and Hβ emission lines to ensure a reliable metallicity measurement in each pixel. When we calculate the average metallicity in each bin, three different weight methods are used: (1) unweighted: the metallicity of each pixel is weighted equally; (2) Hα weighted: the metallicity is weighted by the Hα flux at that pixel; (3) inverse variance weighted: the metallicity is weighted by the inverse variance of the metallicity at that pixels. The Hα weighted method can lower the weights on the pixels that have low flux, however it can potentially bias the average metallicity. Similarly, the inverse variance weighted method can increase the weights of the pixels with more accurate metallicity measurements.

We then fit the resulting metallicity–radius relation using ordinary least squares linear regression, implemented via the `curve_fit` function from the SCIPY library (P. Virtanen et al. 2020), to obtain both the metallicity gradient and central metallicity. We normalized the gradient by the R_e of the galaxy to remove the size dependence of metallicity gradients (S. F. Sánchez et al. 2014; I. T. Ho et al. 2015; L. Sánchez-Menguiano et al. 2016; H. Poetrodjojo et al. 2021).

Figs 2 and 3 show examples of the resolved metallicity map and metallicity gradient for two galaxies in the sample (MAGPIID 1203195161, MAGPIID 1508217276). The uncertainties were determined from the linear fitting process, performed using the `curve_fit` function. This fitting routine accounts for the uncertainties in the average metallicity of individual bins, which were propagated through the fitting procedure to yield the uncertainty on the gradient. We also show the Hα, [N II], and [O II] flux distribution from the models made by BLOBBY3D in Appendix A.

We investigate how the spatial extent of galaxies affects the reliability of metallicity gradient measurements. Fig. 4 shows the distribution of the radius of the most extended radial bin (r_{max}) relative to $\mathrm{PSF_{FWHM}}$ and to R_e. The majority (59/70) of our sample have gradients measured out to at least 1.5 R_e. In our sample selection, we include only those galaxies with gradients measured over a radial extent of at least 2 $\mathrm{PSF_{FWHM}}$, as gradients derived from fewer resolution elements are subject to larger uncertainties. The mean gradient uncertainty of the full sample is 0.01 dex $\mathrm{kpc^{-1}}$. To assess whether small galaxy size affects the accuracy of metallicity gradient measurements, we construct an extended subsample of galaxies with metallicity measured in at least seven radial bins (0.5 $\mathrm{PSF_{FWHM}}$ each bin). For each of these galaxies, we re-fit the

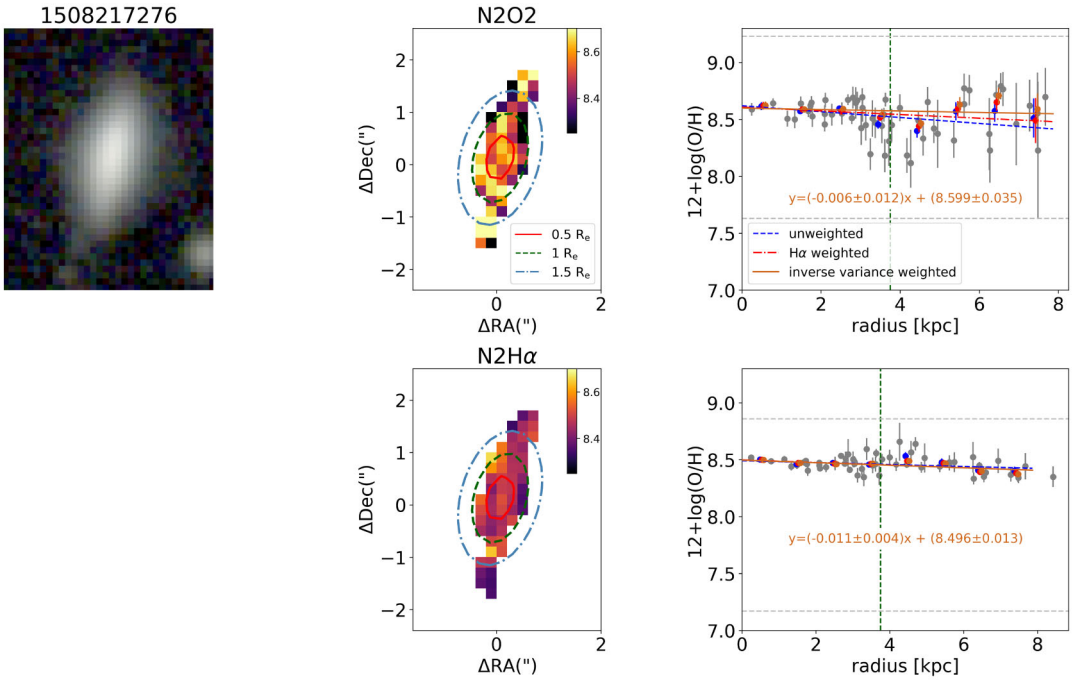

Figure 3. The metallicity and metallicity gradient measurement for an example galaxy (MAGPIID 1508217276). The same as Fig. 2.

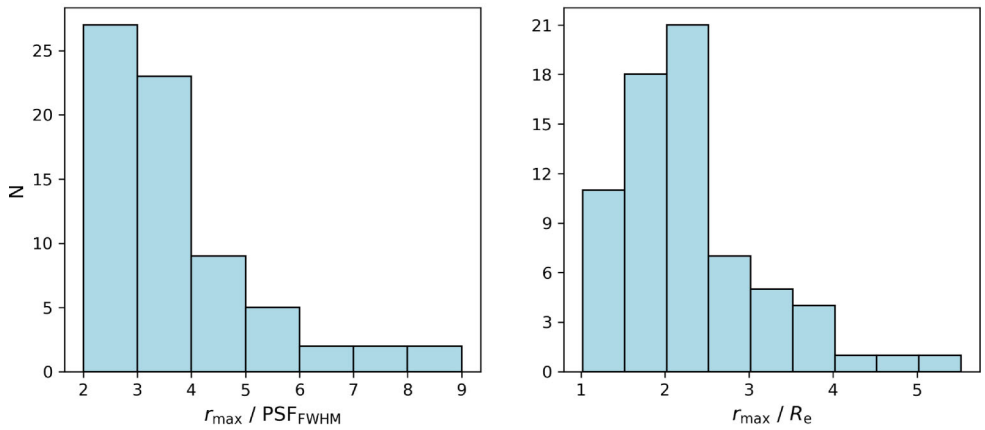

Figure 4. The left panel shows the distribution of the radius of the most extended radial bin (r_{max}) relative to PSF_{FWHM}. The right panel shows the distribution of r_{max} with respect to R_e. Most of the galaxies are moderately resolved, extending out to a median of $R \sim 2\,R_e$.

metallicity gradient using progressively smaller radial ranges, down to four bins. We find good agreement between gradients of the same galaxies measured at small and large radii but with a typical offset of $\nabla[O/H][\geq 7\,\text{bins}] - \nabla[O/H][< 7\,\text{bins}] = 0.02\,\text{dex}\,\text{kpc}^{-1}$. We add this uncertainty in quadrature to the existing uncertainties for gradients measured with <7 bins.

4 RESULTS AND ANALYSIS

The median of the metallicity gradients (N2O2 diagnostic, inverse variance weighted method) is $-0.013^{+0.059}_{-0.033}\,\text{dex}\,\text{kpc}^{-1}$. Among 70 galaxies in our sample, there are 23 galaxies (32.9 per cent) that have significantly negative metallicity gradients (i.e. deviations from zero greater than 2σ), seven galaxies (10.0 per cent) that have significantly positive metallicity gradients and 40 galaxies (57.1 per cent) that have flat gradients (i.e. consistent with zero within 2σ).

We use the metallicity measured with the N2O2 diagnostic and the inverse variance weighted method for the following analysis, unless otherwise specified. A comparison between the N2O2 and N2Hα metallicity gradients is presented in Section 4.2. The metallicity gradients and central metallicities for all galaxies are compiled in Appendix B, with results provided for both the N2O2 and N2Hα diagnostics using the inverse variance weighted method. Using the inverse variance weighted method as our primary approach, we find that the metallicity gradients are consistent with those measured using unweighted and Hα weighted methods. Specifically, 65 out of 70 galaxies are consistent within $0.5\,\sigma$, and all galaxies are consistent within $1\,\sigma$.

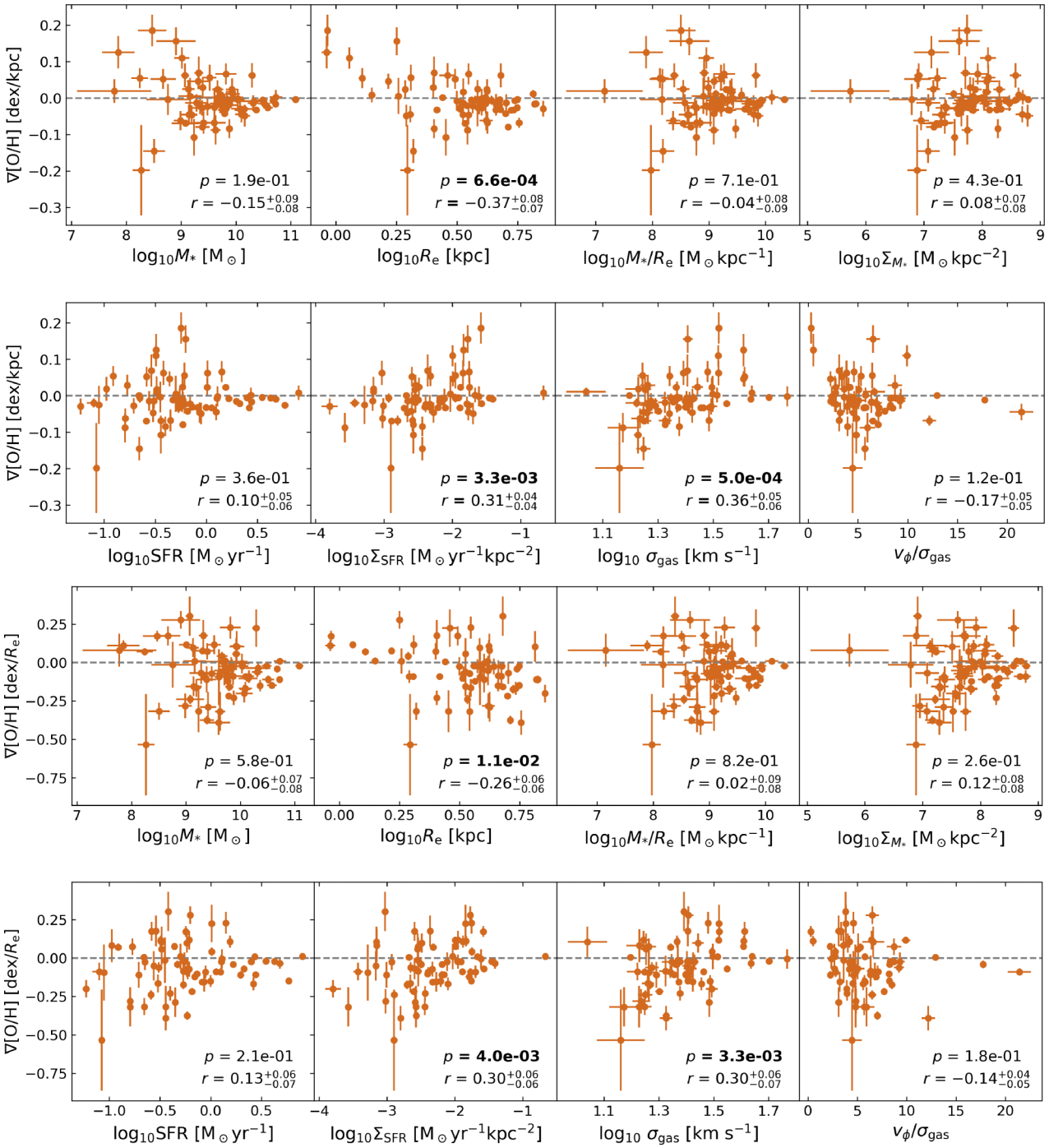

Figure 5. The N2O2 metallicity gradients (top two rows in units of dex/kpc, bottom two rows in units of dex/R_e) as a function of a variety of galaxy properties, including stellar mass (M_*), R_e, a proxy for the gravitational potential (M_*/R_e), Σ_{M_*}, SFR, Σ_{SFR}, σgas, and v_ϕ/σ_{gas}. We show the Pearson correlation coefficient, r, and p-value on each panel. The horizontal dashed lines denote the flat gradient. The ∇[O/H] of MAGPI galaxies has a moderately significant positive correlation with σ_{gas} and with Σ_{SFR} and negative correlation with R_e.

4.1 Correlation between metallicity gradient and galaxy properties

To understand the mechanisms that influence metallicity gradients, we investigate the relation between metallicity gradient and several galaxy properties, including stellar mass (M_*), R_e, a proxy for the gravitational potential (M_*/R_e), Σ_{M_*}, SFR, Σ_{SFR}, σgas, and the ratio between rotational velocity and gas velocity dispersion (v_ϕ/σ_{gas}).We show the relationship between the metallicity gradient (∇[O/H]) and galaxy properties in Fig. 5. For each data point, we sample metallicity gradient and galaxy property values from a normal distribution centred on the measured value with a standard deviation equal to the uncertainty. We repeat this process 1000 times and calculate the Pearson correlation coefficient, r, for each resample. We show the median of r and 16th and 84th percentiles of r on each panel. We also show p-value, which helps determine whether

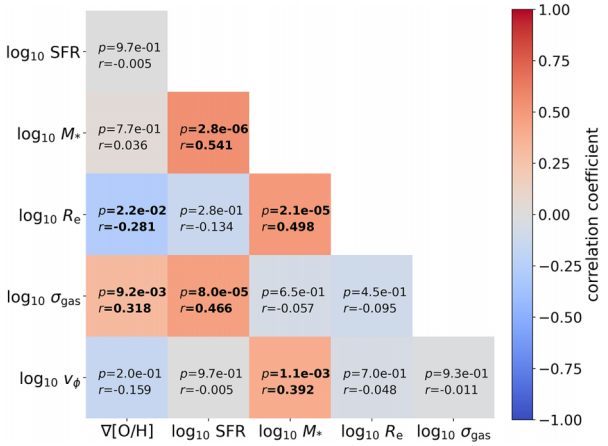

Figure 6. The Pearson partial correlation between ∇[O/H], SFR, M_*, R_e, σ_{gas}, and v_ϕ for MAGPI galaxies. The correlation coefficient (r) and p-value are shown in each box.

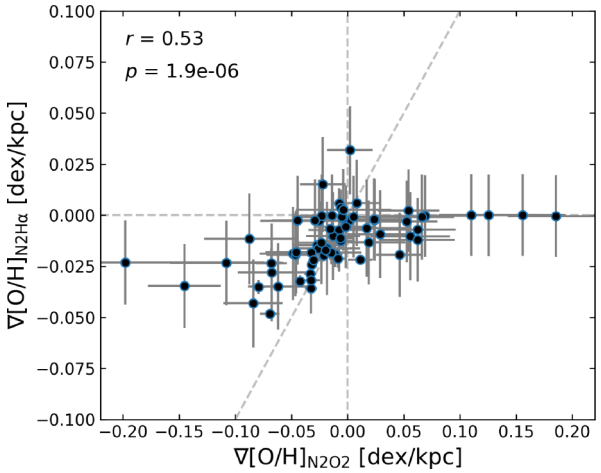

Figure 7. The comparison of the metallicity gradients measured using N2O2 and N2H α diagnostics. The diagonal dashed line indicates the one-to-one relation. The correlation coefficient (r) and p-value are shown in the top left. The metallicity gradients measured using two diagnostics are significantly correlated ($r = 0.53$, $p = 1.9 \times 10^{-6}$), though data show substantial scatter around the one-to-one line.

the observed correlation is statistically significant. A p-value of 0.05 or lower is generally considered statistically significant. We show metallicity gradients in units of dex kpc^{-1} in the top two rows, and in units of dex/R_e in the bottom two rows. The results are similar for metallicity gradients in different units. We discuss our results in units of dex kpc^{-1}.

We find the ∇[O/H] of MAGPI galaxies has a moderately significant positive correlation with σ_{gas} ($r = 0.36^{+0.05}_{-0.06}$, $p = 5.0 \times 10^{-4}$) and with Σ_{SFR} ($r = 0.31^{+0.04}_{-0.04}$, $p = 3.3 \times 10^{-3}$). R_e is negatively correlated with the ∇[O/H] of MAGPI galaxies ($r = -0.37^{+0.08}_{-0.07}$, $p = 6.6 \times 10^{-4}$). There is no significant correlation between ∇[O/H] and other parameters ($|r| < 0.2$ and $p > 0.05$).

To disentangle the intercorrelation between different parameters, we also analyse the partial correlation (J. Whittaker 2009; S. Kim 2015) between ∇[O/H], SFR, M_*, R_e, σ_{gas}, and v_ϕ. We calculate the Pearson partial correlation coefficient for each pair of parameters and p-value using PINGOUIN (R. Vallat 2018). The partial correlation quantifies the linear relationship between two variables while statistically controlling for the influence of all other variables in the sample. This approach isolates the direct association between each pair of parameters, independent of any shared correlations with the remaining variables. We consider the correlation to be significant when $p < 0.05$. As shown in Fig. 6, ∇[O/H] has the strongest partial correlation with σ_{gas}. In addition to σ_{gas}, R_e has a negative correlation with ∇[O/H]. The correlation between ∇[O/H] and M_*, SFR and v_ϕ is not significant when accounting for the correlation with σ_{gas}.

4.2 Comparison of the N2O2 and N2H α diagnostics

We compare the N2O2 and N2H α metallicity gradients in Fig. 7. While the metallicity gradients measured using these two diagnostics are significantly correlated ($r = 0.53$, $p = 1.9 \times 10^{-6}$), they exhibit substantial scatter and deviate from the one-to-one line. These differences may arise from the differing sensitivity of the two diagnostics to variations in ionization parameter and ISM pressure (e.g. H. Poetrodjojo et al. 2021).

Our results show that different metallicity diagnostics predict different metallicity distributions in some galaxies. For example, in galaxy MAGPIID 1203 195 161 (Fig. 2) the metallicity decreases with radius smoothly in the N2O2 diagnostic, while in the N2H α diagnostic, the metallicity decreases within 4 kpc and then slightly increases between 4–7 kpc and decreases again at the larger radii. The variation of ionization parameter and ISM pressure across the galaxy may play a role in the increase of the metallicity profile, as the N2H α diagnostic is sensitive to ionization parameter and sensitive to ISM pressure at high metallicities. Therefore, assuming a constant log(U) limits the accuracy of the N2H α diagnostic. This finding aligns with H. Poetrodjojo et al. (2021), who showed that the metallicity gradients derived using different diagnostics present systematic discrepancies. H. Poetrodjojo et al. (2021) reported a Spearman rank correlation coefficient of $\rho = 0.59$ between the N2O2 and N2H α metallicity gradients, which is comparable in strength to the Pearson correlation we measure ($r = 0.53$).

Our results are comparable to the findings of B. Easeman et al. (2022), who explored the origin of dips in radial metallicity profiles using various diagnostics. While they did not find a clear link between these dips and the variation of ionization parameter, they proposed that inside-out quenching could be a possible driver. In our sample, some galaxies have elevated N2H α metallicity in their centres or their outer discs. This may link to inside-out quenching or outside-in quenching, which depends on the environment (e.g. D. Wang et al. 2022). Further studies are needed to investigate how the variation of ionization parameter and quenching scenarios influences the metallicity measured using different diagnostics.

While the strength of the correlations differs, the trends in metallicity gradients derived from N2H α and N2O2 are broadly consistent in direction. The N2H α metallicity gradient in the unit of dex/kpc shows a weak positive correlation with σ_{gas} ($r = 0.20^{+0.09}_{-0.10}$, $p = 9.3 \times 10^{-3}$) and Σ_{SFR} ($r = 0.22^{+0.08}_{-0.09}$, $p = 4.5 \times 10^{-3}$). Compared with the N2O2 metallicity gradient, the N2H α gradient has no significant correlation with R_e ($r = -0.12^{+0.11}_{-0.10}$, $p = 8.5 \times 10^{-2}$).

We show the comparison of the central metallicity derived from the two calibrations in Fig. 8. The central metallicities measured using the N2O2 and N2H α diagnostics are tightly correlated ($r = 0.91$, $p = 3.7 \times 10^{-28}$). The N2O2 diagnostic yields ∼0.2 dex higher metallicities than N2H α at the high-metallicity end, while the two diagnostics give consistent results around $12 + \log(O/H) \sim 8.3$. At the low-metallicity end, the N2O2 diagnostic predicts slightly lower metallicities. Overall, the relation between the N2O2- and

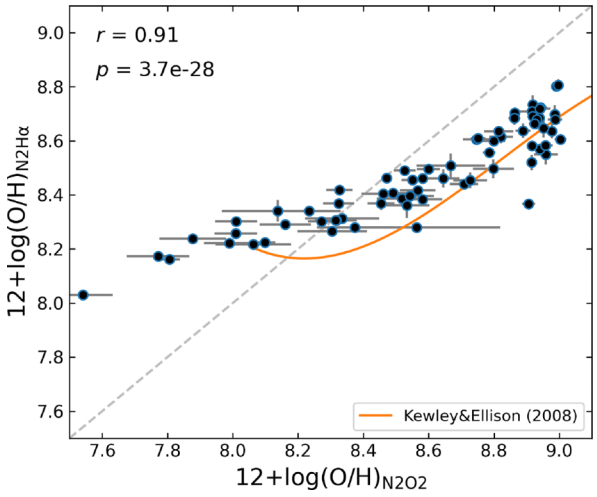

Figure 8. The comparison of the central metallicity measured using N2O2 and N2H α diagnostics. The diagonal dashed line indicates the one-to-one relation. The correlation coefficient (r) and p-value are shown in the top left. The solid line shows the empirical calibration conversion between N2O2 and N2H α from L. J. Kewley & S. L. Ellison (2008). The two diagnostics are tightly correlated ($r = 0.91$, $p = 3.7 \times 10^{-28}$), with N2O2 yielding systematically higher metallicities by $\sim$0.2 dex at the high-metallicity end and slightly lower values at the low-metallicity end. The trend is consistent with the empirical calibration conversion by L. J. Kewley & S. L. Ellison (2008).

N2H α-based metallicities is consistent with the empirical calibration conversion determined by L. J. Kewley & S. L. Ellison (2008).

4.3 The influence of seeing on MAGPI metallicity gradient measurements

The modelling technique we used accounts for the effect of seeing and has a large flexibility in the flux distribution. We compare the seeing-deconvolved metallicity gradient measured from the flux map output of BLOBBY3D with the seeing-convolved metallicity gradient measured from the flux map output of GIST, in Fig. 9. As expected, we see that the seeing-convolved metallicity gradients are flatter than the seeing-deconvolved gradients (T. T. Yuan et al. 2013; J. P. Stott et al. 2014; E. Wuyts et al. 2016; F. Belfiore et al. 2017; A. Acharyya et al. 2020). The seeing-convolved gradients are closer to seeing-deconvolved gradients when the galaxies are large compared to the seeing. The difference is negligible ($\Delta(\nabla[O/H]) < 0.014$ dex kpc^{-1}) for galaxies with gradients measured beyond $r_{max}/PSF_{FWHM} \geqslant 6$, as shown in the right panel of Fig. 9. For well-resolved galaxies, the difference between seeing-convolved and deconvolved gradients is minor. For more compact galaxies, however, the impact of seeing could be significant, making it essential to account for PSF effects in studies of metallicity gradients.

5 DISCUSSION

5.1 Drivers of the metallicity gradient

The MAGPI galaxies in our sample show mildly negative metallicity gradients on average, a trend that is generally interpreted as a consequence of disc inside-out growth, where the central regions experience longer star formation and enrichment than the outskirts (R. B. Larson 1976; F. Matteucci & P. Francois 1989; S. Boissier & N. Prantzos 1999). However, a substantial fraction of galaxies display flat gradients, and a smaller fraction even positive gradients, pointing to the influence of additional processes.

Galaxies can have a steep negative metallicity gradient if the metals stay undisturbed in the galactic disc (B. K. Gibson et al. 2013). However, mechanisms like gas inflows, outflows, accretion, galaxy interaction, and mergers play a role in redistributing the metals in the galaxy, which can flatten or even invert the metallicity gradient (G. Cresci et al. 2010; L. J. Kewley et al. 2010; D. S. N. Rupke et al. 2010; F. Marinacci et al. 2014; J. Chisholm et al. 2018). The positive correlation between ∇[O/H] and σ_{gas} of the MAGPI galaxies (Fig. 5) suggests a connection between gas turbulence and metallicity gradient flattening. Y. Mai et al. (2024) found that the main driver of gas turbulence in the MAGPI galaxies is stellar feedback or gas instability. They found that σ_{gas} has the strongest correlation with Σ_{SFR} and the second strongest correlation with the non-rotational motion of gas (e.g. gas bulk inflows and outflows), suggesting that gas accretion and transportation also contribute to gas turbulence in the MAGPI galaxies. This result agrees with the model for metallicity gradients developed by P. Sharda et al. (2024), which showed that stellar feedback, gas accretion and transportation are important to drive gas turbulence and metal-mixing. Only models that include those mechanisms can reproduce the ∇[O/H]–M_* relation in the local galaxies.

The connection between gas velocity dispersion and metallicity gradients has been reported in high-redshift galaxies. J. Queyrel et al. (2012) found a weak positive correlation ($r = 0.26$) in a sample of 26 galaxies at $z \sim 1.2$. In comparison, our sample at $z \sim 0.3$ yields a stronger correlation ($r = 0.36$) based on 70 galaxies. Similarly, P. Sharda et al. (2021b) compiled a sample of 74 high-redshift galaxies ($0.1 \leq z \leq 2.5$) from multiple ground-based IFU measurements and found that most of the dispersion-dominated galaxies ($v_\phi/\sigma_{gas} \leq 1$, where v_ϕ is the rotational velocity) have flat gradients, while the rotation-dominated galaxies have both flat gradients and steep negative gradients. However, we find the relation between ∇[O/H] and v_ϕ/σ_{gas} is insignificant in the MAGPI sample.

Our result also shows that galaxies with higher Σ_{SFR} have flatter or positive metallicity gradients (Fig. 5). This trend is consistent with the scenario that the accretion of pristine gas or gas transportation from the outskirts to the inner regions flattens or inverts the metallicity gradient and triggers star formation (D. S. N. Rupke et al. 2010; J. P. Stott et al. 2014). The galaxies with positive metallicity gradients might result from metal-poor IGM accreting directly to the centre of the galaxy, which dilutes the central metallicity and inverts the metallicity gradient (G. Cresci et al. 2010). High values of Σ_{SFR} are also linked to a high likelihood of the presence of star-formation driven winds (e.g. C. L. Martin 2005; D. S. Rupke, S. Veilleux & D. B. Sanders 2005; T. M. Heckman & S. Borthakur 2016), which can dilute gradients. Partial correlation analysis (Fig. 6) shows that the ∇[O/H]–Σ_{SFR} relation is largely driven by the underlying dependence on galaxy size, with compact galaxies (small R_e) more likely to exhibit flat or positive gradients. This suggests that the mechanisms that redistribute metals are likely more efficient in smaller galaxies.

The relative strength of different mechanisms may vary with stellar mass. We find a bend in the ∇[O/H]–M_* relation in our sample, with the minimum around 10^{10} M$_\odot$, as shown in Fig. 10. Observations of local galaxies suggest that the mass–metallicity gradient relation reaches a minimum at $\sim 10^{10}$ M$_\odot$ for N2O2-based gradients (or $\sim 10^{10.5}$ M$_\odot$ for N2H α gradients), i.e. the metallicity gradient decreases with increasing stellar mass when $M_* \lesssim 10^{10}$ M$_\odot$ and increases with increasing stellar mass when $M_* \gtrsim 10^{10}$ M$_\odot$ (F. Belfiore et al. 2017; M. Mingozzi et al. 2020; H. Poetrodjojo et al.

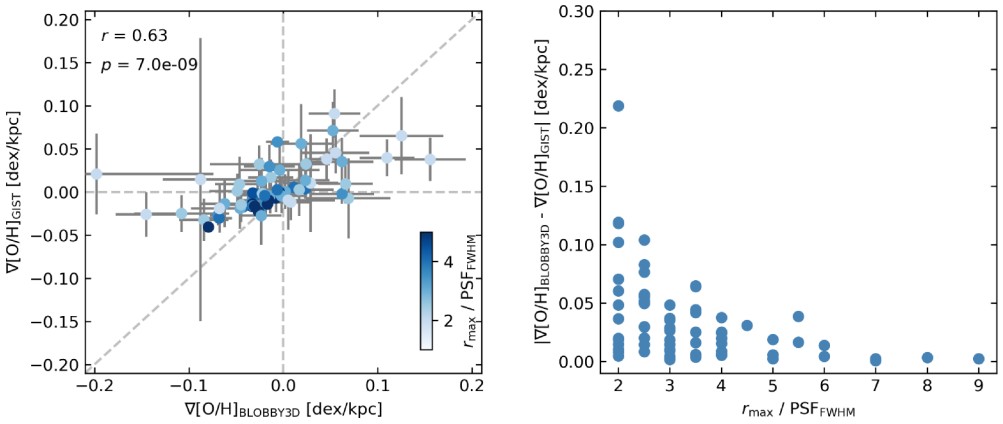

Figure 9. Left: Comparison of seeing-convolved (∇[O/H]$_{\rm GIST}$) and seeing-deconvolved (∇[O/H]$_{\rm BLOBBY3D}$) metallicity gradients of the MAGPI galaxies, colour-coded by the ratio between the radius of the maximum radial bin ($r_{\rm max}$) and the FWHM of PSF. The correlation coefficient (r) and p-value are shown in the top left. Right: The difference between ∇[O/H]$_{\rm GIST}$ and ∇[O/H]$_{\rm BLOBBY3D}$ versus $r_{\rm max}$/PSF$_{\rm FWHM}$.

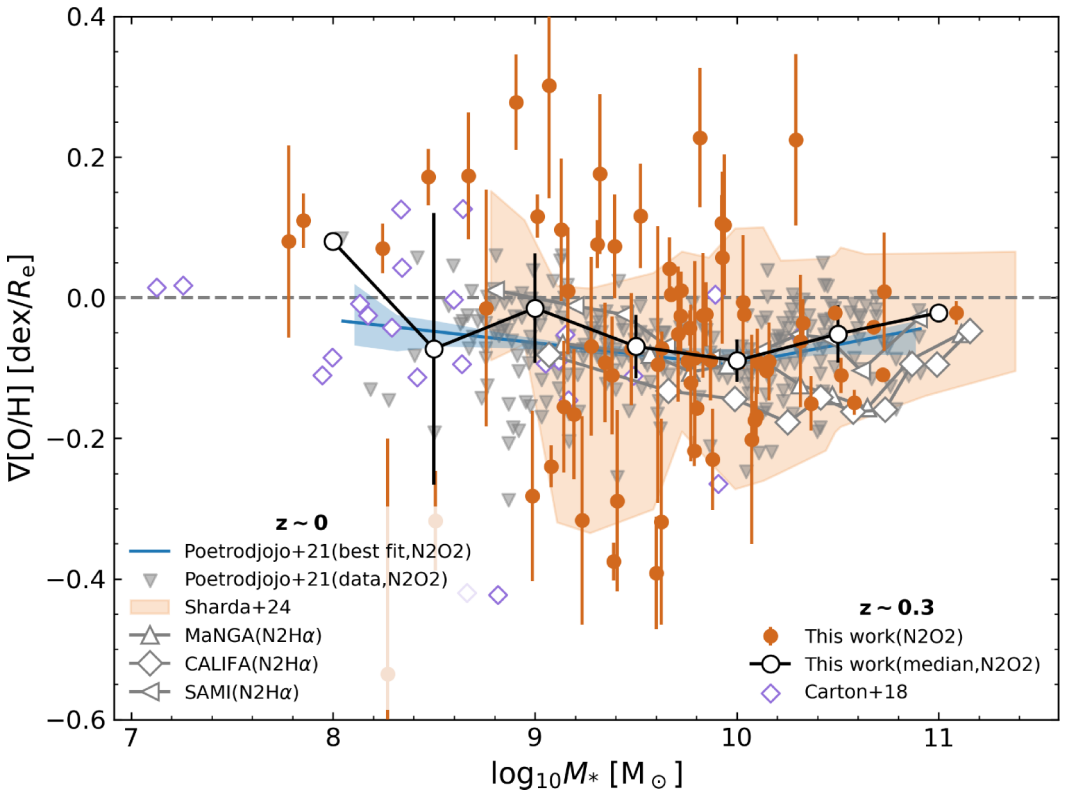

Figure 10. The ∇[O/H]–M_* relation for galaxies at $z \sim 0.3$ and $z \sim 0$. The galaxies of the MAGPI survey are shown as solid circles. The median ∇[O/H] in each 0.3 dex M_* bin are shown as edge-outlined circles. The galaxies at the same redshift range as this study ($0.26 < z < 0.42$) measured by D. Carton et al. (2018) are shown as open diamonds. The galaxies of the SAMI survey at $z \sim 0$ are shown as solid triangles (N2O2 diagnostic) and their best fit (a broken linear-fit) is shown as a solid line and the 1σ uncertainty is indicated by the shaded region. The model prediction from P. Sharda et al. (2024) for the galaxies in the local Universe is shown as a shaded band. The galaxies in the local Universe from the SAMI (H. Poetrodjojo et al. 2021), MaNGA (F. Belfiore et al. 2017), and CALIFA (S. F. Sánchez et al. 2014) surveys are shown as edge-outlined markers, with seeing-correction made by A. Acharyya (2022). Note that the metallicity of galaxies in the SAMI, MaNGA, and CALIFA surveys shown as edge-outlined markers is measured using the N2Hα diagnostic.

2021; T. Li et al. 2025). The existence of the bend is insensitive to the choice of the metallicity diagnostic (H. Poetrodjojo et al. 2021). Theoretical models presented in P. Sharda et al. (2024) explored the relative contribution of stellar feedback, gas accretion, transportation and winds in shaping metallicity profiles. They proposed the following physical interpretation for this behaviour in local galaxies: (1) In low-mass galaxies ($M_* \lesssim 10^{9.5}$ M$_\odot$), metal mixing processes, such as gas accretion and feedback-driven outflows, dominate over *in situ* metal production, resulting in relatively flat or even inverted metallicity gradients. (2) In intermediate-mass galaxies ($10^{9.5} \lesssim M_* \lesssim 10^{10.5}$ M$_\odot$), metal production becomes more efficient, while radial gas flows are weaker, leading to steeper metallicity gradients. (3) In high-mass galaxies ($M_* \gtrsim 10^{10.5}$ M$_\odot$), gas accretion and transportation again become dominant over metal

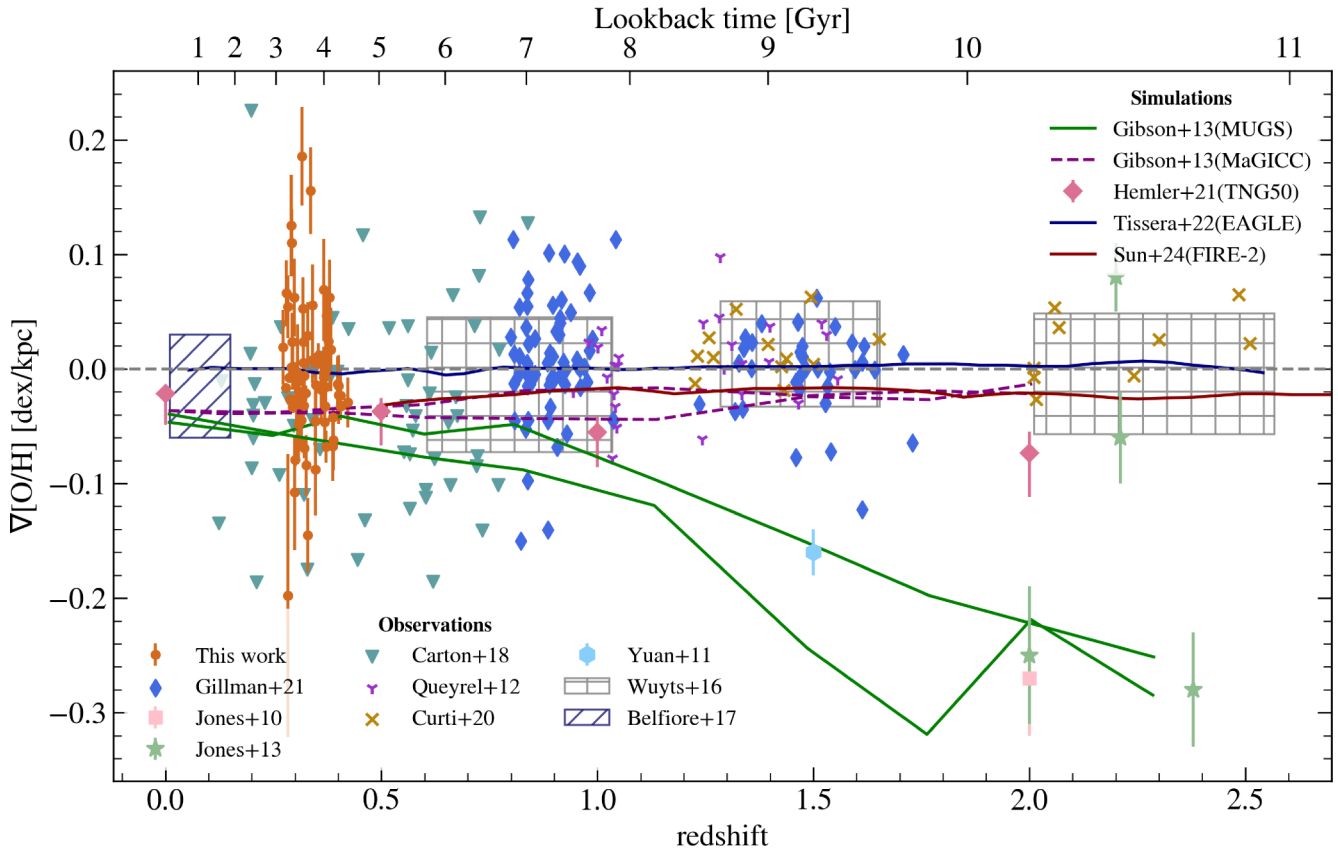

Figure 11. The redshift evolution of the metallicity gradient from previous studies and this work. We compile simulation results from B. K. Gibson et al. (2013), Z. S. Hemler et al. (2021), P. B. Tissera et al. (2022), and X. Sun et al. (2025). We also include observational studies results from S. Gillman et al. (2021), D. Carton et al. (2018), E. Wuyts et al. (2016), F. Belfiore et al. (2017), T. Jones et al. (2010, 2013), T. T. Yuan et al. (2011), J. Queyrel et al. (2012), and M. Curti et al. (2020). We note that the regions with diagonal and cross-hatching show the range of metallicity gradient and redshift in F. Belfiore et al. (2017) and E. Wuyts et al. (2016), respectively. The metallicity gradient shows only mild evolution with redshift, while a large intrinsic scatter is present at all epochs.

production, leading to the flattening of metallicity gradients at the high-mass end.

We compare the ∇[O/H]–M_* relation of the MAGPI galaxies with galaxies at the same redshift[2] ($z \sim 0.3$; D. Carton et al. 2018), galaxies at $z \sim 0$, and the theoretical predictions for local galaxies from P. Sharda et al. (2024), with the mass-loading factor in the model estimated from the EAGLE cosmological simulations (P. D. Mitchell et al. 2020), as shown in Fig. 10. The ∇[O/H]–M_* relation of the MAGPI galaxies qualitatively agrees with the prediction by P. Sharda et al. (2024). The MAGPI galaxies have similar metallicity gradients on average to the galaxies in the SAMI, MaNGA, and CALIFA samples (all at $z \sim 0$). However, the scatter and uncertainty of the metallicity gradient are large in our low-mass bins ($M_* \leq 10^{9.5}$ M$_\odot$). The model in P. Sharda et al. (2024) shows that the metallicity gradient of low-mass galaxies ($M_* \lesssim 10^{9.5}$ M$_\odot$) varies significantly with the extent of newly produced metals mixing with the ISM (described by the yield reduction factor, ϕ_y[3]). The low-mass bins in our sample are dominated by positive or flat metallicity gradients, consistent with local dwarf samples (T. Li et al. 2025). Such positive gradients may arise from the accretion of metal-poor gas (G. Cresci et al. 2010) or feedback-driven outflows, as has been suggested for dwarf galaxies (M. Grossi et al. 2020; T. Li et al. 2025). A larger sample, or higher spatial resolution, is needed to confirm this result.

5.2 Evolution of metallicity gradient

Most of the observational and simulation studies show that the evolution of metallicity gradients is mild with redshift (e.g. E. Wuyts et al. 2016; S. Gillman et al. 2021; Z. S. Hemler et al. 2021; P. B. Tissera et al. 2022; X. Sun et al. 2025). However, there is a higher fraction of galaxies displaying positive metallicity gradients at $z \gtrsim 1$ than at $z \sim 0$ (G. Cresci et al. 2010; E. Wuyts et al. 2016; D. Carton et al. 2018; S. Gillman et al. 2021). We compile metallicity gradient measurements from previous studies, in combination with our results, in Fig. 11. The metallicity gradients of the MAGPI galaxies generally agree with previous observations (D. Carton et al. 2018) and simulations (B. K. Gibson et al. 2013; P. B. Tissera et al. 2022; X. Sun et al. 2025) results at the same redshift.

Among all observational studies presented in Fig. 11, only D. Carton et al. (2018) and this work employ the forward modelling approach to account for beam smearing. In this study, we model the flux distributions of individual emission lines and subsequently derive the metallicity gradient, whereas D. Carton et al. (2018) directly modelled the metallicity gradient. Both E. Wuyts et al. (2016) and S. Gillman et al. (2021) modelled the impact of beam smearing

[2]Note that the redshift range of the galaxies in D. Carton et al. (2018) is $0.1 \lesssim z \lesssim 0.8$. We only select galaxies from their sample that are in the same redshift range as this study ($0.26 < z < 0.42$).

[3]$0 \leq \phi_y \leq 1$. $\phi_y \sim 1$ means the newly produced metals from supernovae are fully mixed with ISM before ejected and $\phi_y \sim 0$ means the newly produced metals are ejected from the galaxy without mixing with ISM.

as a function of different observational and intrinsic parameters and applied corrections to each galaxy based on their model. The scatter of the metallicity gradients of our result is similar to the results in D. Carton et al. (2018), but notably larger than the seeing convolved results. We also note that we are able to measure metallicity gradients down to stellar masses much lower ($<10^9$ M$\odot$) than those of the studies at $z \gtrsim 1$.

The divergence of the metallicity gradient predictions is obvious for galaxies at $z \gtrsim 1$. B. K. Gibson et al. (2013) demonstrated the evolution of the metallicity gradient of two types of feedback models, as shown in Fig. 11. MaGICC (Making Galaxies in a Cosmological Context; C. B. Brook et al. 2012) is the 'enhanced' feedback model, which is efficient in redistributing the metals over large scales and flattening the metallicity gradient at high redshift. MUGS (McMaster Unbiased Galaxy Simulations; G. S. Stinson et al. 2010) is the 'conventional' feedback model, which employed a weaker feedback scheme than MaGICC, returning much steeper metallicity gradients for galaxies at high redshift. We note that the stellar mass range of the galaxies in MaGICC and MUGS simulation is comparable to the MAGPI data we use.

It is unclear which of these two feedback models best describes the observed metallicity gradients at $z \sim 0.3$. However, our result shows that the galaxies with higher $\sigma_{\rm gas}$ have flatter metallicity gradients, suggesting a connection between the strength of feedback and metallicity gradient flattening. The driver of higher $\sigma_{\rm gas}$ and the flattening of the metallicity gradient may be the same.

Most of the observations of high redshift galaxies showed shallow-to-flat metallicity gradient (Fig. 11), which agrees with higher $\sigma_{\rm gas}$ and stronger gas transportation and accretion in higher redshift galaxies (E. Wisnioski et al. 2015; H. Übler et al. 2019; Y. Mai et al. 2024). However, the flat gradients at high redshift may result from the limit of resolution and the flattening caused by the seeing (T. T. Yuan et al. 2013; F. Belfiore et al. 2017), as we discuss in Section 4.3.

6 CONCLUSIONS

We measured the seeing-deconvolved gas-phase metallicity of 70 SF galaxies at $z \sim 0.3$ from the MAGPI survey. We used a Bayesian inference method, BLOBBY3D, to model the flux distribution of different emission lines. This method takes the effect of seeing into account and has high flexibility with regard to the flux distribution. We calculated the metallicity using the N2O2 and N2Hα diagnostics (K19). We summarize the main findings below.

(i) The median N2O2 metallicity gradient of our sample is $-0.013^{+0.059}_{-0.033}$ dex kpc^{-1}. Among the 70 galaxies, 32.9 per cent exhibit significant ($\geq 2\sigma$) negative gradients, 10.0 per cent show significant positive gradients, and 57.1 per cent are consistent with flat gradients, the latter likely driven by turbulence and feedback-induced mixing.

(ii) The ∇[O/H]–M_* relation of the MAGPI galaxies is generally consistent with the theoretical prediction of P. Sharda et al. (2024), which suggests that multiple mechanisms, including stellar feedback, gas transportation and gas accretion, contribute to the shaping of the metallicity profile, and the relative importance of these mechanisms varies with the stellar mass of galaxies. However, the scatter and uncertainty of metallicity gradients of low-mass galaxies are large in our sample. Further study with a large sample is needed to understand the variation of metallicity gradients at $z \sim 0.3$.

(iii) The N2O2 metallicity gradients (measured in units of dex kpc^{-1}) are positively correlated with $\sigma_{\rm gas}$ ($r = 0.36^{+0.05}_{-0.06}$) and $\Sigma_{\rm SFR}$ ($r = 0.31^{+0.04}_{-0.04}$). The metallicity gradients also have a negative correlation with $R_{\rm e}$ ($r = -0.37^{+0.08}_{-0.07}$). Partial correlation analysis shows that $\sigma_{\rm gas}$ exhibits the strongest correlation with the metallicity gradients, followed by $R_{\rm e}$, while SFR shows no significant correlation. Galaxies with higher gas turbulence tend to have flatter or even positive metallicity gradients. These results suggest that mechanisms driving gas turbulence, such as stellar feedback, gas accretion, and transportation, enhance gas mixing, thereby leading to flattened or inverted metallicity gradients. In addition, smaller galaxies may be more susceptible to the accretion of metal-poor gas, or stellar feedback-driven outflows, and thus exhibit inverted (positive) metallicity gradients.

(iv) The metallicity gradients measured using N2O2 and N2Hα diagnostics are broadly consistent ($r = 0.53$). Some galaxies have dips in their radial N2Hα metallicity profiles or show elevated central N2Hα metallicity compared to N2O2 measurements. The difference between them may result from the variation of the ionization parameter and ISM pressure.

(v) Metallicity gradients show only a mild evolution with redshift. The significant scatter observed at all epochs may arise from variations in galaxy mass, size, star formation activity, or environment.

(vi) We confirm that the seeing-convolved metallicity gradients are flatter than the seeing-deconvolved metallicity gradients. This effect is mitigated when the size of galaxies is large ($>6\times$) compared to the seeing.

Overall, our results demonstrate that metallicity gradients at $z \sim 0.3$ are shaped by a combination of internal and external processes such as star formation, stellar feedback, gas accretion, and transportation. The correlation with gas turbulence highlights the importance of gas mixing processes in redistributing metals. While the ∇[O/H]–M_* relation suggests that the balance of these mechanisms evolves with stellar mass.

Future work will aim to expand the galaxy sample, especially at the low-mass end, where the large scatter and uncertainties limit robust conclusions. A larger data set will improve statistical constraints on metallicity gradients and enable a clearer assessment of the relative roles of stellar feedback, gas accretion, internal gas transport, and environmental effects, and how these processes vary with stellar mass. Future IFU surveys with higher spatial resolution and sensitivity, enabled by upcoming AO-assisted instruments, e.g. the Multi-conjugate Adaptive-optics Visible Imager-Spectrograph (MAVIS; R. M. McDermid et al. 2020) on the VLT, the Giant Magellan Telescope integral fields spectrograph and imager (GMTIFS; R. Sharp et al. 2016), and the High Angular Resolution Monolithic Optical and Near-infrared Integral field spectrograph (HARMONI; N. Thatte et al. 2021), will be essential to push metallicity gradient studies to higher redshifts and smaller spatial scales.

ACKNOWLEDGEMENTS

We wish to thank the ESO staff, and in particular the staff at Paranal Observatory, for carrying out the MAGPI observations. MAGPI targets were selected from GAMA. GAMA is a joint European–Australasian project based around a spectroscopic campaign using the Anglo-Australian Telescope. GAMA was funded by the STFC (UK), the ARC (Australia), the AAO, and the participating institutions. GAMA photometry is based on observations made with ESO Telescopes at the La Silla Paranal Observatory under programme ID 179.A-2004, ID 177.A-3016. The MAGPI team acknowledge support by the Australian Research Council Centre of Excellence for All Sky Astrophysics in 3 Dimensions (ASTRO 3D), through project no. CE170100013. YM is supported by an Australian Government Research Training Program (RTP) Scholarship. LMV acknowledges support by the German Academic

Scholarship Foundation (Studienstiftung des deutschen Volkes) and the Marianne-Plehn-Program of the Elite Network of Bavaria. IB has received funding from the European Union's Horizon 2020 research and innovation programme under the Marie Sklodowska-Curie Grant agreement ID no.°101059532. This project was extended for six months by the Franziska Seidl Funding Program of the University of Vienna. SMS acknowledges funding from the Australian Research Council (DE220100003). Parts of this research were conducted by the Australian Research Council Centre of Excellence for All Sky Astrophysics in 3 Dimensions (ASTRO 3D), through project no. CE170100013. KH acknowledges support by the Royal Society through a Dorothy Hodgkin Fellowship to KA Oman (DHF/R1/231105). TG acknowledges support from ARC Discovery Project DP210101945. CF is the recipient of an Australian Research Council Future Fellowship (project no. FT210100168) funded by the Australian Government. CF is a recipient of ARC Discovery Project DP210101945. PS is supported by the Leiden University Oort Fellowship and the International Astronomical Union – Gruber Foundation (TGF) Fellowship.

DATA AVAILABILITY

The MUSE data used in this work are available on the ESO public archive. The reduced MAGPI datacubes and the emission line data products will be public in the MAGPI team data release (Mendel et al., in preparation and Battisti et al., in preparation).

REFERENCES

Acharyya A., 2022, Doctoral thesis. The Australian National University. Available at: https://openresearch-repository.anu.edu.au/server/api/core/bitstreams/fd8e9347-aad6-46d2-ab33-89129d074e55/content
Acharyya A., Krumholz M. R., Federrath C., Kewley L. J., Goldbaum N. J., Sharp R., 2020, MNRAS, 495, 3819
Acker A., Köppen J., Samland M., Stenholm B., 1989, The Messenger, 58, 44
Bacon R. et al., 2010, in McLean I. S., Ramsay S. K., Takami H., eds, Proc. SPIE Conf. Ser. Vol. 7735, Ground-based and Airborne Instrumentation for Astronomy III. SPIE, Bellingham, p. 773508
Bacon R. et al., 2017, A&A, 608, A1
Baker W. M. et al., 2025, Nat. Astron., 9, 141
Baldwin J. A., Phillips M. M., Terlevich R., 1981, PASP, 93, 5
Barbani F., Pascale R., Marinacci F., Torrey P., Sales L. V., Li H., Vogelsberger M., 2025, A&A, 697, A121
Belfiore F. et al., 2017, MNRAS, 469, 151
Bellstedt S. et al., 2020, MNRAS, 498, 5581
Bittner A. et al., 2019, A&A, 628, A117
Boissier S., Prantzos N., 1999, MNRAS, 307, 857
Bouché N., Carfantan H., Schroetter I., Michel-Dansac L., Contini T., 2015, AJ, 150, 92
Brewer B. J., Foreman-Mackey D., 2018, J. Stat. Softw., 86, 1
Brewer B. J., Pártay L. B., Csányi G., 2011, Stat. Comput., 21, 649
Brook C. B., Stinson G., Gibson B. K., Wadsley J., Quinn T., 2012, MNRAS, 424, 1275
Bruzual G., Charlot S., 2003, MNRAS, 344, 1000
Bundy K. et al., 2015, ApJ, 798, 7
Cappellari M., 2017, MNRAS, 466, 798
Cappellari M., Emsellem E., 2004, PASP, 116, 138
Carton D. et al., 2017, MNRAS, 468, 2140
Carton D. et al., 2018, MNRAS, 478, 4293
Chabrier G., 2003, PASP, 115, 763
Charlot S., Fall S. M., 2000, ApJ, 539, 718
Chiappini C., Matteucci F., Romano D., 2001, ApJ, 554, 1044
Chisholm J., Tremonti C., Leitherer C., 2018, MNRAS, 481, 1690
Choi J., Dotter A., Conroy C., Cantiello M., Paxton B., Johnson B. D., 2016, ApJ, 823, 102
Collacchioni F., Lagos C. D. P., Mitchell P. D., Schaye J., Wisnioski E., Cora S. A., Correa C. A., 2020, MNRAS, 495, 2827
Conroy C., Gunn J. E., 2010, ApJ, 712, 833
Conroy C., Gunn J. E., White M., 2009, ApJ, 699, 486
Conroy C., White M., Gunn J. E., 2010, ApJ, 708, 58
Courteau S., 1997, AJ, 114, 2402
Cresci G., Mannucci F., Maiolino R., Marconi A., Gnerucci A., Magrini L., 2010, Nature, 467, 811
Curti M. et al., 2020, MNRAS, 492, 821
Davies R. et al., 2011, ApJ, 741, 69
Di Teodoro E. M., Fraternali F., 2015, MNRAS, 451, 3021
Driver S. P. et al., 2011, MNRAS, 413, 971
Easeman B., Schady P., Wuyts S., Yates R. M., 2022, MNRAS, 511, 371
Falcón-Barroso J. et al., 2006, MNRAS, 369, 529
Fitzpatrick E. L., Massa D., Gordon K. D., Bohlin R., Clayton G. C., 2019, ApJ, 886, 108
Foster C. et al., 2021, PASA, 38, e031
Fu J., Hou J. L., Yin J., Chang R. X., 2009, ApJ, 696, 668
Fusco T. et al., 2020, A&A, 635, A208
Gibson B. K., Pilkington K., Brook C. B., Stinson G. S., Bailin J., 2013, A&A, 554, A47
Gillman S. et al., 2021, MNRAS, 500, 4229
Gordon K., 2024, dust_extinction, Zenodo, Version v1.4.1, Zenodo. Available at: https://doi.org/10.5281/zenodo.11235336
Grand R. J. J. et al., 2019, MNRAS, 490, 4786
Grossi M., García-Benito R., Cortesi A., Gonçalves D. R., Gonçalves T. S., Lopes P. A. A., Menéndez-Delmestre K., Telles E., 2020, MNRAS, 498, 1939
Gurvich A. B. et al., 2023, MNRAS, 519, 2598
Heckman T. M., Borthakur S., 2016, ApJ, 822, 9
Hemler Z. S. et al., 2021, MNRAS, 506, 3024
Ho I. T., Kudritzki R.-P., Kewley L. J., Zahid H. J., Dopita M. A., Bresolin F., Rupke D. S. N., 2015, MNRAS, 448, 2030
Jones T., Ellis R., Jullo E., Richard J., 2010, ApJ, 725, L176
Jones T., Ellis R. S., Richard J., Jullo E., 2013, ApJ, 765, 48
Ju M. et al., 2025, ApJ, 978, L39
Kassin S. A. et al., 2012, ApJ, 758, 106
Kauffmann G. et al., 2003, MNRAS, 346, 1055
Kennicutt Robert C. J., 1998, ARA&A, 36, 189
Kepner J. V., 1999, ApJ, 520, 59
Kereš D., Katz N., Weinberg D. H., Davé R., 2005, MNRAS, 363, 2
Kewley L. J., Ellison S. L., 2008, ApJ, 681, 1183
Kewley L. J., Dopita M. A., Sutherland R. S., Heisler C. A., Trevena J., 2001, ApJ, 556, 121
Kewley L. J., Rupke D., Zahid H. J., Geller M. J., Barton E. J., 2010, ApJ, 721, L48
Kewley L. J., Nicholls D. C., Sutherland R. S., 2019, ARA&A, 57, 511 (K19)
Kim S., 2015, Commun. Stat. Appl. Methods, 22, 665
Kobayashi C., Nakasato N., 2011, ApJ, 729, 16
Kohandel M., Pallottini A., Ferrara A., Carniani S., Gallerani S., Vallini L., Zanella A., Behrens C., 2020, MNRAS, 499, 1250
Kohandel M., Pallottini A., Ferrara A., Zanella A., Rizzo F., Carniani S., 2024, A&A, 685, A72
Larson R. B., 1976, MNRAS, 176, 31
Law D. R. et al., 2022, ApJ, 928, 58
Levy R. C. et al., 2018, ApJ, 860, 92
Li T. et al., 2025, A&A, 698, A208
Li Z. et al., 2025, ApJS, 280, 62
Ma X., Hopkins P. F., Feldmann R., Torrey P., Faucher-Giguère C.-A., Kereš D., 2017, MNRAS, 466, 4780
Mai Y. et al., 2024, MNRAS, 533, 3878
Marinacci F., Pakmor R., Springel V., Simpson C. M., 2014, MNRAS, 442, 3745
Martin C. L., 2005, ApJ, 621, 227
Matteucci F., Francois P., 1989, MNRAS, 239, 885
Mayor M., Vigroux L., 1981, A&A, 98, 1

McDermid R. M. et al., 2020, preprint (arXiv:2009.09242)
Metha B., Trenti M., Chu T., 2021, MNRAS, 508, 489
Metha B., Trenti M., Chu T., Battisti A., 2022, MNRAS, 514, 4465
Mingozzi M. et al., 2020, A&A, 636, A42
Mitchell P. D., Schaye J., Bower R. G., Crain R. A., 2020, MNRAS, 494, 3971
Mollá M., Díaz A. I., 2005, MNRAS, 358, 521
Mun M. et al., 2024, MNRAS, 530, 5072
Muratov A. L., Kereš D., Faucher-Giguère C.-A., Hopkins P. F., Quataert E., Murray N., 2015, MNRAS, 454, 2691
Osterbrock D. E., 1989, Astrophysics of Gaseous Nebulae and Active Galactic Nuclei. University Science Books, Mill Valley, CA, p. 408
Parlanti E., Carniani S., Pallottini A., Cignoni M., Cresci G., Kohandel M., Mannucci F., Marconi A., 2023, A&A, 673, A153
Peng C. Y., Ho L. C., Impey C. D., Rix H.-W., 2002, AJ, 124, 266
Péroux C., Howk J. C., 2020, ARA&A, 58, 363
Pettini M., Pagel B. E. J., 2004, MNRAS, 348, L59
Pezzulli G., Fraternali F., 2016, MNRAS, 455, 2308
Pilkington K. et al., 2012, A&A, 540, A56
Poetrodjojo H., D'Agostino J. J., Groves B., Kewley L., Ho I. T., Rich J., Madore B. F., Seibert M., 2019, MNRAS, 487, 79
Poetrodjojo H. et al., 2021, MNRAS, 502, 3357
Portinari L., Chiosi C., 1999, A&A, 350, 827
Queyrel J. et al., 2012, A&A, 539, A93
Rizzo F., Vegetti S., Fraternali F., Stacey H. R., Powell D., 2021, MNRAS, 507, 3952
Rizzo F., Kohandel M., Pallottini A., Zanella A., Ferrara A., Vallini L., Toft S., 2022, A&A, 667, A5
Robotham A. S. G. et al., 2011, MNRAS, 416, 2640
Robotham A. S. G., Bellstedt S., Lagos C. d. P., Thorne J. E., Davies L. J., Driver S. P., Bravo M., 2020, MNRAS, 495, 905
Rupke D. S., Veilleux S., Sanders D. B., 2005, ApJS, 160, 115
Rupke D. S. N., Kewley L. J., Barnes J. E., 2010, ApJ, 710, L156
Sánchez-Menguiano L. et al., 2016, A&A, 587, A70
Sánchez S. F. et al., 2014, A&A, 563, A49
Sarzi M. et al., 2006, MNRAS, 366, 1151
Schlafly E. F., Finkbeiner D. P., 2011, ApJ, 737, 103
Sérsic J. L., 1963, Bol. Asociacion Argentina Astron. Plata Argentina, 6, 41
Sharda P., Krumholz M. R., Wisnioski E., Forbes J. C., Federrath C., Acharyya A., 2021a, MNRAS, 502, 5935
Sharda P., Wisnioski E., Krumholz M. R., Federrath C., 2021b, MNRAS, 506, 1295
Sharda P., Ginzburg O., Krumholz M. R., Forbes J. C., Wisnioski E., Mingozzi M., Zovaro H. R. M., Dekel A., 2024, MNRAS, 528, 2232
Sharp R. et al., 2016, in Evans C. J., Simard L., Takami H., eds, Proc. SPIE Conf. Ser. Vol. 9908, Ground-based and Airborne Instrumentation for Astronomy VI. SPIE, Bellingham, p. 99081Y
Skilling J., 2004, in Fischer R., Preuss R., Toussaint U. V., eds, AIP Conf. Proc. Vol. 735, Bayesian Inference and Maximum Entropy Methods in Science and Engineering: 24th International Workshop on Bayesian Inference and Maximum Entropy Methods in Science and Engineering. Am. Inst. Phys., New York, p. 395
Stinson G. S., Bailin J., Couchman H., Wadsley J., Shen S., Nickerson S., Brook C., Quinn T., 2010, MNRAS, 408, 812
Stott J. P. et al., 2014, MNRAS, 443, 2695
Sun X. et al., 2025, ApJ, 986, 179
Thater S. et al., 2022, MNRAS, 509, 5416
Thatte N. et al., 2021, The Messenger, 182, 7
Tissera P. B., Rosas-Guevara Y., Sillero E., Pedrosa S. E., Theuns T., Bignone L., 2022, MNRAS, 511, 1667
Troncoso P. et al., 2014, A&A, 563, A58
Übler H. et al., 2019, ApJ, 880, 48
Übler H. et al., 2024, MNRAS, 527, 9206
Vallat R., 2018, J. Open Source Softw., 3, 1026
Vallini L. et al., 2024, MNRAS, 527, 10
Varidel M. R. et al., 2019, MNRAS, 485, 4024
Veilleux S., Maiolino R., Bolatto A. D., Aalto S., 2020, A&AR, 28, 2
Venturi G. et al., 2024, A&A, 691, A19
Virtanen P. et al., 2020, Nat. Methods, 17, 261
Wang D. et al., 2022, MNRAS, 516, 3411
Wang X. et al., 2022, ApJ, 938, L16
Whittaker J., 2009, Graphical Models in Applied Multivariate Statistics. Wiley Publ., New York
Wisnioski E. et al., 2015, ApJ, 799, 209
Wright R. J., Somerville R. S., Lagos C. d. P., Schaller M., Davé R., Anglés-Alcázar D., Genel S., 2024, MNRAS, 532, 3417
Wuyts E. et al., 2016, ApJ, 827, 74
Yates R. M., Henriques B. M. B., Fu J., Kauffmann G., Thomas P. A., Guo Q., White S. D. M., Schady P., 2021, MNRAS, 503, 4474
Yuan T. T., Kewley L. J., Swinbank A. M., Richard J., Livermore R. C., 2011, ApJ, 732, L14
Yuan T. T., Kewley L. J., Rich J., 2013, ApJ, 767, 106

APPENDIX A: BLOBBY3D EMISSION-LINE FLUX MAPS

We show the 2D flux maps of the BLOBBY3D results for two MAGPI galaxies in our sample (MAGPIID 1203195161, MAGPIID 1508217276) in Figs A1 and A2. These maps illustrate the emission-line flux distributions derived from the BLOBBY3D forward-modelling process, which simultaneously fits the kinematics and spatial distribution of each line while accounting for the effects of seeing.

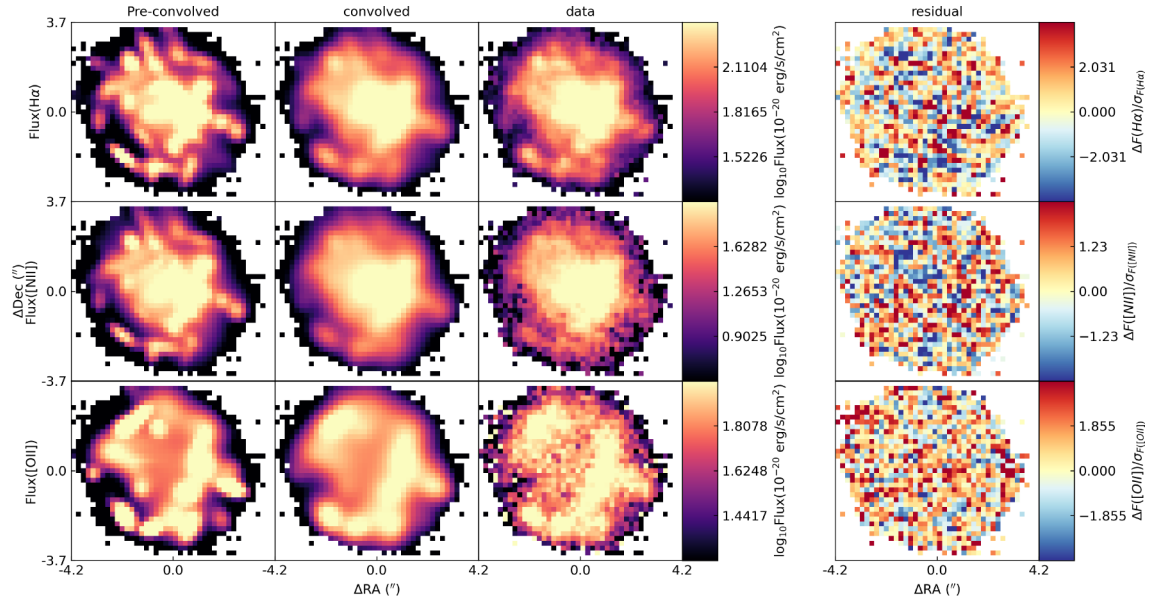

Figure A1. The 2D flux maps from the BLOBBY3D model and observational data for MAGPI galaxy 1203195161. The first column shows the seeing-deconvolved flux distribution from the model, the second column shows the corresponding seeing-convolved model flux, the third column shows the flux map obtained from a single-Gaussian fit to the observed data cube, and the fourth column shows the residuals between the observed data and the seeing-convolved model. The first, second, and third rows correspond to the H α, [N II] and [O II] lines, respectively.

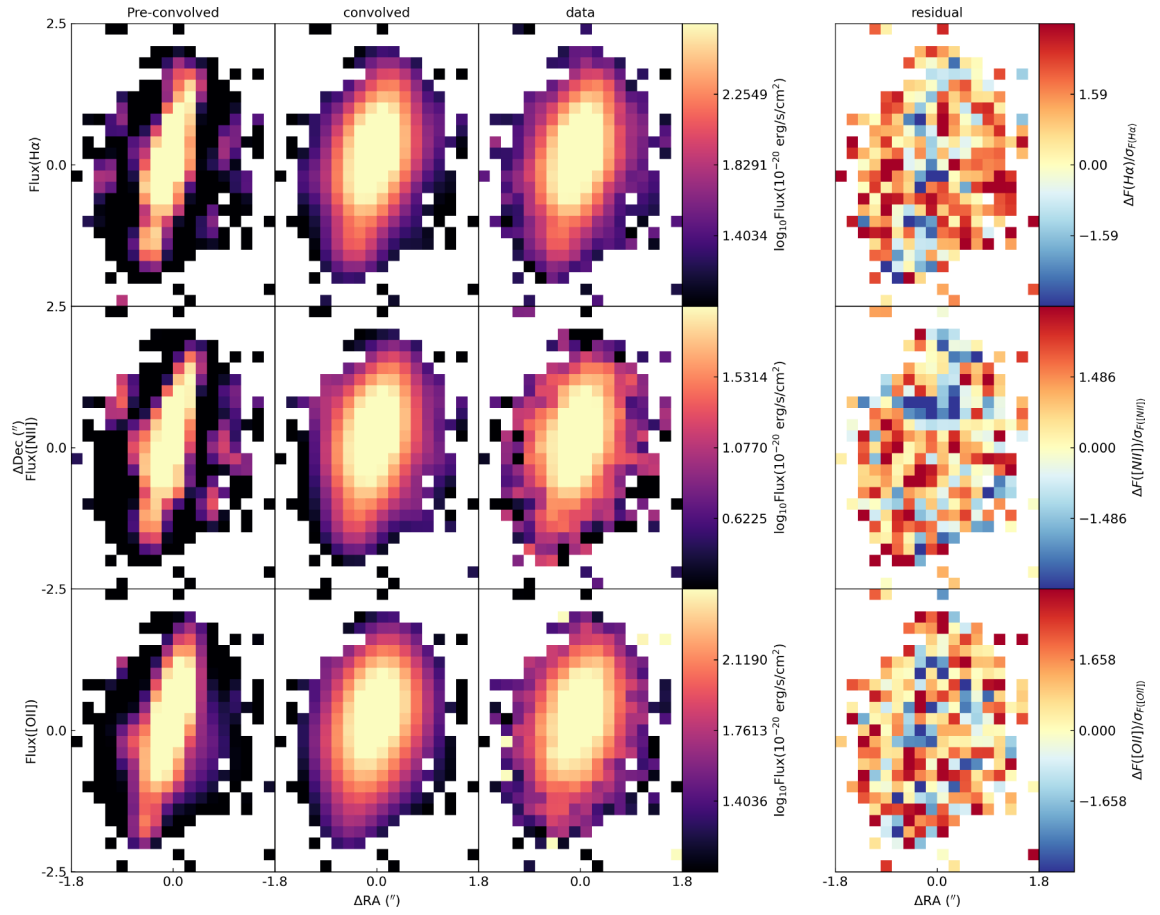

Figure A2. Same as Fig. A1, but for MAGPI galaxy 1508217276.

APPENDIX B: COMPILED DATA

We list the metallicity gradient and central metallicity measured using the N2O2 and N2H α diagnostics, and galaxy properties for 70 galaxies in our sample in Table B1.

Table B1. (1) Target name, (2–3) Metallicity gradient and central metallicity measured using the N2O2 diagnostic, (4–5) Metallicity gradient and central metallicity measured using the N2H α diagnostic, (6) Stellar mass, (7) SFR, (8) Intrinsic ionized gas velocity dispersion taken from Y. Mai et al. (2024), (9) Effective radius measured from i-band image, (10) Redshift.

MAGPIID	Gradient (N2O2) [dex kpc^{-1}]	Central (N2O2) $12 + \log_{10}$(O/H)	Gradient (N2H α) [dex kpc^{-1}]	Central (N2H α) $12 + \log_{10}$(O/H)	$\log_{10} M_*$ [M$_\odot$]	SFR [M$_\odot$ yr^{-1}]	$\sigma_{\rm gas}$ [km s^{-1}]	$R_{\rm e}$ [kpc]	z
1201302222	-0.108 ± 0.050	8.374 ± 0.117	-0.023 ± 0.021	8.280 ± 0.015	9.23	0.36	16.89	2.85	0.30
1202077074	-0.013 ± 0.024	8.645 ± 0.049	-0.010 ± 0.021	8.461 ± 0.033	9.28	0.59	25.94	5.04	0.40
1203076068	-0.009 ± 0.008	8.821 ± 0.036	-0.021 ± 0.004	8.615 ± 0.025	10.33	4.79	43.22	4.20	0.31
1203191233	0.011 ± 0.011	8.582 ± 0.046	-0.022 ± 0.001	8.461 ± 0.007	9.94	0.33	10.96	6.52	0.35
1203195161	-0.017 ± 0.001	8.996 ± 0.005	-0.018 ± 0.003	8.806 ± 0.022	10.72	2.77	22.67	6.60	0.28
1203235348	-0.018 ± 0.029	8.798 ± 0.063	-0.016 ± 0.023	8.496 ± 0.035	9.79	0.54	21.13	4.58	0.36
1203247089	-0.004 ± 0.042	8.063 ± 0.116	0.003 ± 0.020	8.218 ± 0.003	8.76	0.35	23.37	3.84	0.31
1205196165	0.001 ± 0.003	8.919 ± 0.012	-0.003 ± 0.004	8.691 ± 0.016	9.67	0.22	15.73	2.75	0.29
1206151090	-0.021 ± 0.007	8.785 ± 0.019	-0.020 ± 0.003	8.557 ± 0.009	9.63	2.13	35.38	3.48	0.32
1206322202	-0.084 ± 0.026	8.454 ± 0.042	-0.043 ± 0.022	8.368 ± 0.024	9.88	0.40	23.83	2.54	0.33
1207181305	-0.032 ± 0.008	8.751 ± 0.023	-0.018 ± 0.002	8.609 ± 0.006	10.37	0.99	30.66	4.57	0.32
1208109039	-0.015 ± 0.003	9.003 ± 0.019	-0.007 ± 0.002	8.606 ± 0.017	10.52	1.96	25.02	6.68	0.37
1501329201	0.019 ± 0.032	7.989 ± 0.078	-0.013 ± 0.020	8.222 ± 0.013	7.78	0.11	16.92	4.20	0.27
1502071104	-0.002 ± 0.027	8.799 ± 0.035	-0.006 ± 0.020	8.599 ± 0.005	10.03	1.29	58.57	4.00	0.37
1502079084	0.056 ± 0.036	8.461 ± 0.067	-0.010 ± 0.022	8.405 ± 0.017	9.52	0.61	17.53	2.04	0.34
1502275236	0.185 ± 0.043	7.541 ± 0.090	-0.000 ± 0.020	8.030 ± 0.000	8.47	0.57	33.12	0.92	0.32
1503316290	0.017 ± 0.037	8.668 ± 0.105	-0.006 ± 0.024	8.508 ± 0.044	9.93	0.33	17.92	3.35	0.38
1504220116	-0.011 ± 0.006	8.888 ± 0.023	-0.019 ± 0.006	8.637 ± 0.027	9.77	0.47	23.15	3.94	0.31
1504328073	0.024 ± 0.025	8.324 ± 0.048	-0.002 ± 0.020	8.368 ± 0.004	9.13	0.58	27.71	3.84	0.38
1506082320	0.023 ± 0.025	8.272 ± 0.041	-0.002 ± 0.020	8.302 ± 0.003	9.67	1.02	31.21	1.93	0.29
1506106169	-0.030 ± 0.002	8.991 ± 0.007	-0.022 ± 0.002	8.802 ± 0.012	10.15	0.73	25.06	3.25	0.29
1507211057	-0.045 ± 0.023	8.987 ± 0.022	-0.002 ± 0.022	8.679 ± 0.019	10.10	1.25	17.70	2.03	0.32
1508217276	-0.006 ± 0.012	8.599 ± 0.035	-0.011 ± 0.004	8.496 ± 0.013	9.85	1.27	26.90	3.75	0.30
1508336146	0.029 ± 0.029	8.491 ± 0.046	-0.009 ± 0.021	8.408 ± 0.017	9.39	0.17	18.34	2.52	0.33
1509152248	-0.062 ± 0.027	8.727 ± 0.052	-0.035 ± 0.021	8.454 ± 0.029	8.99	0.16	17.19	4.17	0.39
1509257282	-0.029 ± 0.022	8.906 ± 0.019	-0.002 ± 0.020	8.367 ± 0.001	10.07	0.06	31.11	7.16	0.42
1509291230	0.062 ± 0.034	8.234 ± 0.097	-0.007 ± 0.001	8.340 ± 0.002	10.29	1.02	33.03	2.89	0.30
1511160258	-0.033 ± 0.005	8.943 ± 0.021	-0.029 ± 0.003	8.723 ± 0.015	10.09	0.54	18.55	5.28	0.29
1512115127	-0.069 ± 0.009	8.820 ± 0.026	-0.048 ± 0.003	8.615 ± 0.011	9.08	0.26	17.80	3.41	0.32
1513187164	-0.022 ± 0.020	8.916 ± 0.006	0.015 ± 0.023	8.581 ± 0.016	9.77	0.69	25.56	3.67	0.32
1513284105	0.005 ± 0.050	8.304 ± 0.106	-0.001 ± 0.020	8.266 ± 0.001	9.16	0.50	31.42	1.81	0.32
1514079248	-0.027 ± 0.021	8.518 ± 0.077	-0.015 ± 0.002	8.386 ± 0.010	9.38	0.20	19.54	4.00	0.30
1516091250	0.046 ± 0.021	8.472 ± 0.011	-0.019 ± 0.021	8.463 ± 0.007	9.31	0.44	40.64	1.65	0.37
1517143230	-0.007 ± 0.001	8.977 ± 0.007	0.006 ± 0.004	8.636 ± 0.027	10.68	1.66	22.96	5.48	0.29
1517159274	-0.033 ± 0.008	8.940 ± 0.033	-0.032 ± 0.003	8.719 ± 0.016	10.10	2.63	28.53	5.42	0.41
1517265320	-0.079 ± 0.006	8.940 ± 0.018	-0.035 ± 0.003	8.569 ± 0.020	9.39	0.59	21.21	5.13	0.30
1519062299	-0.015 ± 0.027	8.137 ± 0.170	-0.018 ± 0.006	8.341 ± 0.039	9.71	0.27	25.29	4.15	0.40
1519164262	-0.023 ± 0.025	8.582 ± 0.059	-0.000 ± 0.020	8.384 ± 0.013	9.48	0.61	25.68	3.28	0.40
1523135170	0.023 ± 0.009	8.551 ± 0.034	-0.002 ± 0.002	8.456 ± 0.008	9.92	1.55	23.22	4.19	0.32
1524292106	-0.145 ± 0.032	8.708 ± 0.043	-0.035 ± 0.021	8.440 ± 0.009	8.51	0.22	17.70	2.09	0.33
1528310241	-0.006 ± 0.012	8.527 ± 0.033	-0.013 ± 0.004	8.490 ± 0.013	9.72	0.22	22.22	4.39	0.32
1529336091	0.110 ± 0.029	8.327 ± 0.040	0.000 ± 0.020	8.418 ± 0.000	9.01	0.32	32.98	1.14	0.29
1530070238	-0.008 ± 0.027	8.917 ± 0.039	-0.007 ± 0.020	8.708 ± 0.010	9.83	0.55	26.57	3.15	0.37
1530093302	0.069 ± 0.045	7.771 ± 0.096	-0.000 ± 0.020	8.173 ± 0.000	9.32	0.29	25.46	2.54	0.37
1530272149	-0.020 ± 0.013	8.814 ± 0.044	-0.017 ± 0.001	8.636 ± 0.006	9.87	0.08	16.68	4.72	0.31
1530322331	-0.004 ± 0.003	8.863 ± 0.019	-0.002 ± 0.004	8.685 ± 0.025	11.09	3.51	50.32	5.60	0.37
1531103073	-0.088 ± 0.040	8.542 ± 0.073	-0.012 ± 0.022	8.395 ± 0.025	9.63	0.16	14.88	3.49	0.35
1531178256	-0.014 ± 0.021	8.958 ± 0.021	-0.000 ± 0.020	8.582 ± 0.005	10.31	0.31	18.82	3.35	0.35
1532240333	0.062 ± 0.033	7.877 ± 0.103	-0.012 ± 0.021	8.237 ± 0.017	9.07	0.38	24.64	4.79	0.38
1532282113	0.066 ± 0.029	8.566 ± 0.055	-0.001 ± 0.021	8.417 ± 0.014	9.82	1.41	30.18	3.52	0.28
1533161121	-0.032 ± 0.002	8.939 ± 0.007	-0.024 ± 0.004	8.684 ± 0.019	9.80	0.82	23.64	4.78	0.41
1534070145	-0.049 ± 0.030	8.746 ± 0.041	-0.019 ± 0.023	8.605 ± 0.020	10.16	0.89	21.94	1.95	0.31
1534194077	-0.006 ± 0.003	8.952 ± 0.012	0.004 ± 0.009	8.647 ± 0.035	10.49	4.24	25.32	3.62	0.31

Table B1 – *continued*

MAGPIID	Gradient (N2O2) [dex kpc^{-1}]	Central (N2O2) $12 + \log_{10}$(O/H)	Gradient (N2H α) [dex kpc^{-1}]	Central (N2H α) $12 + \log_{10}$(O/H)	$\log_{10} M_*$ [$M_\odot$]	SFR [$M_\odot$ yr^{-1}]	$\sigma_{\rm gas}$ [km s^{-1}]	$R_{\rm e}$ [kpc]	z
1534261263	-0.046 ± 0.026	8.318 ± 0.053	-0.019 ± 0.020	8.306 ± 0.015	9.19	0.30	18.19	3.52	0.37
1534282147	0.052 ± 0.027	8.010 ± 0.064	-0.003 ± 0.020	8.302 ± 0.005	8.67	0.26	41.00	3.11	0.32
1535157300	-0.023 ± 0.022	7.806 ± 0.032	-0.013 ± 0.020	8.162 ± 0.014	9.35	0.58	25.91	3.90	0.41
2301064121	0.002 ± 0.020	8.916 ± 0.013	0.032 ± 0.022	8.520 ± 0.028	10.73	2.73	32.66	4.13	0.29
2301109255	-0.005 ± 0.002	8.931 ± 0.009	-0.001 ± 0.007	8.679 ± 0.036	10.04	2.51	23.82	4.74	0.29
2302280234	0.125 ± 0.044	8.161 ± 0.078	0.000 ± 0.020	8.290 ± 0.000	7.85	0.32	40.67	0.92	0.29
2304104201	-0.026 ± 0.003	8.987 ± 0.017	-0.016 ± 0.003	8.698 ± 0.034	10.58	5.86	25.45	5.59	0.29
2304202299	0.156 ± 0.050	8.009 ± 0.065	0.000 ± 0.021	8.258 ± 0.000	8.91	0.63	25.57	1.78	0.34
2305332151	-0.025 ± 0.024	8.335 ± 0.114	-0.003 ± 0.021	8.313 ± 0.001	9.61	0.09	18.36	3.84	0.31
2305342325	-0.068 ± 0.008	8.959 ± 0.036	-0.023 ± 0.004	8.550 ± 0.037	9.60	0.36	21.19	5.70	0.37
2308076271	-0.042 ± 0.011	8.925 ± 0.017	-0.032 ± 0.001	8.663 ± 0.018	9.79	0.65	20.04	5.01	0.39
2308129329	-0.068 ± 0.001	8.534 ± 0.068	-0.028 ± 0.003	8.361 ± 0.046	9.41	0.45	30.49	4.22	0.39
2308186140	-0.046 ± 0.029	8.316 ± 0.064	-0.018 ± 0.023	8.306 ± 0.010	9.14	0.86	26.53	3.34	0.35
2310037140	0.008 ± 0.042	8.864 ± 0.004	0.006 ± 0.020	8.704 ± 0.011	9.72	8.02	43.66	1.41	0.34
2310137110	0.054 ± 0.003	8.099 ± 0.032	0.002 ± 0.004	8.224 ± 0.004	8.24	0.12	22.03	1.28	0.28
2310293123	-0.198 ± 0.007	8.563 ± 0.256	-0.023 ± 0.003	8.280 ± 0.013	8.27	0.08	14.49	1.97	0.28
2311102063	-0.033 ± 0.026	8.918 ± 0.012	-0.036 ± 0.022	8.733 ± 0.036	9.76	1.13	29.10	2.61	0.37

This paper has been typeset from a TEX/LATEX file prepared by the author.